CRG SHARP
General Report 2017-2022

Jean-Marc Zanotti
Laboratoire Léon Brillouin
CEA Saclay
91191 Gif-sur-Yvette Cedex
France

On October 2017, the ILL instrument IN6 has become a French CRG operated by the Laboratoire Léon Brillouin (LLB). From then, the instrument has been called IN6-SHARP (Spectromètre Hybride Alpes Région Parisienne) until the full rebuilding of the secondary spectrometer ended in April 2021. At that time, the instrument has been called SHARP. In the framework of the ILL Endurance program phase II, SHARP is being upgraded to SHARP$^+$ with the construction of a fully redesigned guide and primary spectrometer. This brand-new instrument will show a counting rate gain of 15 compared to IN6. It will come on-line in April 2024.
The present document reports on the operation of IN6-SHARP and SHARP over the time period 2017-2022 in terms of beam time use and scientific production. Technical details about SHARP and SHARP$^+$ and in particular key evolutions compared to IN6 are given. We show, that the SHARP spectrometer has been an interesting teasing to take patience up to the 2024 delivery of SHARP$^+$. At that time, this brand-new state-of-the-art very competitive instrument, operating as a French CRG A, will fully complement and integrate the ILL ToF instrumental suite.

Contents

I. Contract history and status 2
II. General statistics 3
III. Beam time use 7
IV. Scientific Production and Bibliometric 7
V. Instrument construction, improvements and upgrades: SHARP 8
VI. Instrument upgrades planned in the near future: SHARP$^+$ 10
VII. Technical problems 14
VIII. Relations with ILL services 15
IX. Training program 16
X. Scientific highlights – Abstracts 17
XI. List of experiments 22
XII. List of publications 33
XIII. Scientific highlight – Full text 40

I. Contract history and status

Following the agreement to strengthen the Franco-Swedish cooperation in the field of neutron scattering, the Laboratoire Léon Brillouin (LLB) has undertaken the construction of an inelastic time-of-flight spectrometer. After the announcement of the Orphée reactor shutdown in 2019, the project originally planned at Saclay could be transferred to the Institut Laue Langevin (ILL). This revival took the form of an "A" type CRG contract concluded on September 29th 2017 between the CEA DRF, the CNRS INP and the ILL. From then, IN6 has been operated by a LLB team and the design of a brand new IN6 secondary spectrometer (components from the monochromator up to the detectors) has started. This was the SHARP (Spectromètre Hybride Alpe Région Parisienne) project.

Type of CRG (A, B, C): IN6-SHARP and SHARP are type "A" CRGs.
This means that the spectrometer scientific team acts as *local contact* of all the experiments performed on the instrument: 50% of the ILL beam-time and 50% of the French user's beam time distributed by the scientific selection panel of the 2FDN (Fédération Française de la Diffusion Neutronique). A key point is that in exchange of the 50% ILL beam-time *local contact* duty, the spectrometer is considered as a full ILL instrument and enjoys the ILL maintenance and sample environment services.

Contracting Partners:

- Institut Laue-Langevin (ILL)
- CEA, Direction de la Recherche Fondamentale
- CNRS, Institut de Physique

CRG Contracts:

- 29/09/2017: Contract on the modernization and of the CRG-A instrument IN6.
- 25/06/2021: First Amendment to the Contract on the operation and modernization of the CRG-A Instrument SHARP. This amendment states "Once the ILL instrument upgrade program Endurance phase II has been validated by the ILL Associates, the Parties will meet and discuss the option of modifying and moving the instrument to another beam position before the end of the amendment. After the modification and move of the instrument to another beam position, it shall be operated by the LLB under the name SHARP$^+$". SHARP$^+$ will remain a CRG-A.
- In November 2022: a new amendment will be signed to transfer to ILL the property of the SHARP$^+$ time-of-flight chamber. The 240 ^{3}He Position Sensitive Detectors (PSD) will remain the property of LLB (as in contract signed on 29/09/2017).

CRG Personnel in Charge:

First Responsible:

Dr. Jean-Marc Zanotti, CEA Research Director, Laboratoire Léon Brillouin (CEA-CNRS), CEA Saclay, France.

Second Responsible:

Dr. Quentin Berrod, Chargé de Recherche de Classe Normale (junior scientist), IRIG,/SyMMES (CEA, CNRS, Université Grenoble Alpes), Grenoble.

Technician:

2017-2021: Benoit Homatter, CEA technician, Laboratoire Léon Brillouin (CEA-CNRS), CEA Saclay, France.

After the 2021 departure of B. Homatter, a new CEA technician currently at LLB will move to Grenoble or a new CEA technician will be hired in 2023. In any cases, a CEA technician will be in charge on SHARP$^+$ for the commissioning of the instrument in April 2024. In 2023, a LLB team will come from Saclay for the construction of the SHARP$^+$ primary spectrometer.

II. General statistics

Key Facts:

- The historical LLB practice to do not allow “In House” beam time has been respected on IN6-SHARP (2017-2020) then on SHARP (2021).
- Excellent availability of the IN6-SHARP instrument: 89% of the available beam time offered to users (**Table 1**).
- Fairly balanced use of the instrument by the users with beam-time granted by the ILL and 2FDN scientific committees: ILL (46%) and 2FDN (54%) (**Table 1**).
- The oversubscription on the instrument (**Table 3**) is satisfactory for both the ILL (2.7) and 2FDN (2.6).
- On average, 17 papers with data collected on the instrument are published each year (**Table 3** and **Figure 2**).
- The key players on the spectrometers (IN6-Sharp then SHARP) are college 4, 6 and 7 with almost one third of the beam-time each (**Table 4**).

Beam-time Allocation on IN6-SHARP (2018-2020)

Beam-time is shared equally between ILL and CRG.
ILL beam-time is allocated via the standard ILL public submission process.
CRG beam time is allocated by the Fédération Française de la Neutronique (2FDN) committee.
Proposals are selected on the basis of their scientific merit.
An experimental report on results achieved during granted beam-time is due.
The following table summarizes the partition, during the period 2017-2020, of the requested and allocated beam-time.

IN6-SHARP									
Year	2018			2019		2020		Total	Average
Cycle #	182	183	184	185	186	187	188		
Start date	01/03/2018	22/05/2018	03/09/2018	13/06/2019	28/09/2019	09/01/2020	17/09/2020		
End date	25/04/2018	12/07/2018	28/10/2018	04/08/2019	15/10/2019	29/02/2020	28/09/2020		
Expected Cycle Duration	49	51	55	52	48	48	48	351	
Expected Total Cycle Duration: $S_{Reactor}$	155			100		96			
Reactor Shutdown	2	6	3	2	0	2	0	15	
Total Reactor Shutdown	11			2		2			
Commissioning	9			1		3		13	
Comment Commissioning	4.5 days for CRG and 4.5 days for ILL commissioning after 2017 long shutdown			1 day at reactor restart		1.5 day CRG and 1.5 day ILL reactor restart			
Instrument Failure	3			2		0		5	
Reason For failure	Chopper Electronic Failure			Secondary Shutter failure		Secondary Shutter failure			
Other days lost	2			3		1		6	
Reason day lost	Health Physics tests for bi-decenal instrument clearance after "Instrument Safety File"			Waiting for Health Physics Clearance		Samp. Env. failure (sample licking in furnace)			
Days lost S_L (commissioning included)	25			8		6		39	
Total Research Effective Beamtime: $S_{REBT} = S_{Reactor} - S_{lost}$	130			92		90		312	
Fraction of Research Effective Beam-time: S_{REBT} / $S_{Reactor}$	**84%**			**92%**		**94%**			**89%**
S_{CRG}: CRG Research Effective Beam time	68			54		45		167	
CRG : Fraction of Research Beam-time: S_{CRG}/S_{REBT}	**52%**			**59%**		**50%**			**54%**
S_{ILL}: ILL Research Effective Beam time	60			38		45		143	
ILL : Fraction of Research Beam-time: S_{ILL}/S_{REBT}	**46%**			**41%**		**50%**			**46%**
S_T: Training	2							2	
Training type	HERCULES practical: Soft Matter & Solid State Physics								
Training : Fraction of Effective beam time: S_T/S_{REBT}	2%			0%		0%			1%

Table 1. Beam-time use on IN6-SHARP over the period 2018 to 2020 (numbers are expressed in “days”).

Statistics of the beam-time use are shown on Table 1. The key information is that, on average, 90% of the reactor time has been used for experiments with beam-time granted by the ILL and 2FDN scientific committees. The beam-time use is fairly balanced between the ILL (46%) and 2FDN (54%) users. Strict equality is lost due to a number of experiments cancelled by ILL users. For better readability, an enlarged version of this table can be found in Annex 1.

Beam-time Allocation on SHARP (2021)

SHARP	
Year	2021
Cycle #	191
Start date	24/08/2021
End date	13/10/2021
Expected Cycle Duration	50
Expected Total Cycle Duration: $S_{Reactor}$	50
Reactor Shutdown	0
Total Reactor Shutdown	0
Commissioning	10
Comment Commissioning	Setting the radial collimator after late arrival (Brexit related customs issues)
Instrument Failure	0
Reason For failure	0
Other days lost	0
Reason day lost	
Days lost S_L (commissioning included)	10
Total Research Effective Beamtime: $S_{REBT} = S_{Reactor} - S_{lost}$	40
Fraction of Research Effective Beam-time: $S_{REBT} / S_{Reactor}$	80%
S_{CRG}: CRG Research Effective Beam time	22
CRG : Fraction of Research Beam-time: S_{CRG}/S_{REBT}	55%
S_{ILL}: ILL Research Effective Beam time	16
ILL : Fraction of Research Beam-time: S_{ILL}/S_{REBT}	40%
S_T: Training	2
Training type	FANs du LLB practical: Soft Matter & Solid State Physics
S_T/S_{REFBT}	5%

Table 2. Beam-time use on SHARP during the 2021 "back to users" cycle following the construction and commissioning (numbers are expressed in "days").

Sharp has welcomed its first users with official beam-time on September and October 2021.

The instrument performances have been ranked as very high from all the users.

The beam balance deficit between ILL and 2FDN is due to a late ILL proposal cancelation. It has been replaced by a Grenoble 2FDN "B" proposal.

Altogether, this real running of the new instrument has been important to fully qualify all the elements of the spectrometer along with the adaptation of all the ancillary equipments.

This will be a key for the success of the SHARP$^+$ commissioning phase. As the secondary spectrometer is already validated, the instrument team will have to mainly focus on the primary spectrometer. One can therefore expect the SHARP$^+$ will be able to welcome official users in a very short time after its April 2024 delivery and commissioning.

Nationality Balance of the IN6-SHARP Users.

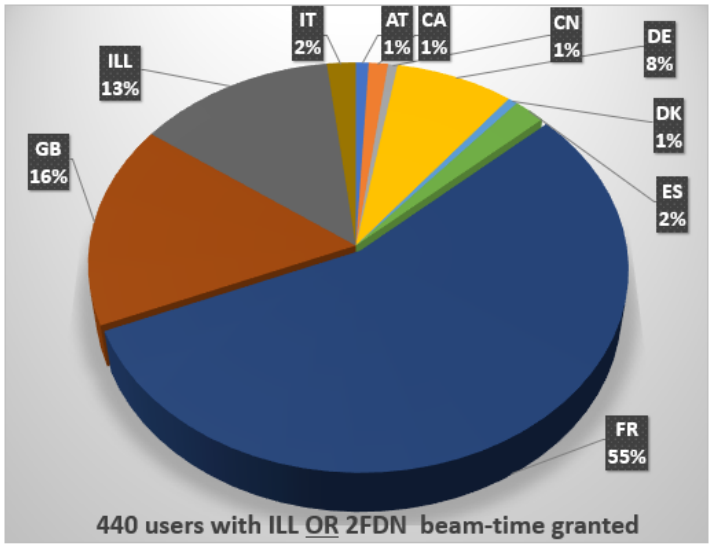

Figure 1. Repartition of the number of users by country of the home Laboratory (the label "ILL" stands for ILL scientists).

a) CRG users are included and all considered as French.

Total number of users = 440.

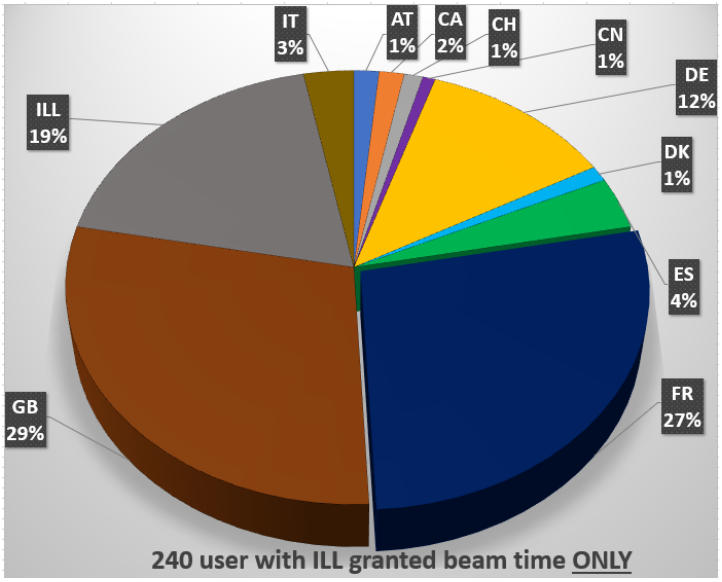

b) Users with CRG beam-time excluded.

Total number of users = 240.

Figure 1 shows the repartition of the number of users by country of the home Laboratory. On the top plot, the CRG users are considered, while on the bottom one they have been excluded. As during the Covid time, most of the experiments have been performed in "remote mode", the number of "effective visitors" on the instrument would be a biased indicator. Therefore, in these statistics, for the whole period 2018-2020, all the names on the proposals have been considered. The apparent deficit of German Laboratories users (12%) compared to English (29%) and French (27%) ones is not real. It is due to a number of English and French proposals showing an inflation of collaborators.

Yearly statistics: number of experiments & users, factor pressure, papers

IN6-SHARP										
YEAR	2018		2019		2020		2021		2022	
	CRG	ILL*	CRG	ILL	CRG	ILL	CRG	ILL	CRG	ILL
Beamtime request	186	80*	129	177	129	151	46	34		
Beamtime granted	71	22*	53	55	53	60	16	14		
Oversubscription	2.6	3.6*	2.4	3.2	2.4	2.5	2.9	2.4		
Number of experiments	16	16**	14	22	15	18	7	5		
Number of publications	12		18		17		17		6 (over January- June)	
Number of users	49	68	58	97	64	52	29	23		
Total Number of users	117		155		116		52			

Table 3. Yearly partition of the requested and allocated beam-time between ILL and CRG, the oversubscription factor, the number of experiments[1] performed, the publications record and the number of users. For "" and "**" values, see footnote below.*

The oversubscription if on average of 2.7 (the factor of 3.6* excluded) for ILL and 2.6 for 2FDN. Above a pressure factor of 3, one usually observes a discouragement of users which leads to a decrease of submitted proposals. Here, these pressure factors are elevated and it is satisfactory that they remain below 3. The number of publications is at a good level in quantity (constant around 17 each year) but also in quality (see **Figure 2**).

		IN6-SHARP & SHARP (2018-2021)					
College #	Field	ILL Beam-Time (Days)	% of ILL Beam-time	CRG Beam-Time (Days)	% of CRG Beam-time	Total (Days)	Total %
1	Applied Materials Science, Instrumentation and Techniques	6	4%			6	2%
2	Theory						
3	Nuclear and Particle Physics						
4	Magnetic excitations	28	**16%**	69	**36%**	97	**28%**
5	Crystallography / Magnetic Structures						
6	Structure and dynamics of disordered systems	31	**18%**	94	**48%**	125	**36%**
7	Spectroscopy in solid state physics & chemistry	90	**59%**	14	**10%**	104	**30%**
8	Structure and dynamics of biological systems			5	3%	5	1%
9	Structure and dynamics of soft-condensed matter	4	3%	7	4%	11	3%
	Total	159	100%	189	100%	348	100%

Table 4. Partition by ILL scientific college of the effective ILL and 2FDN beam-time. This statistic includes the cycle over which SHARP has welcomed users.

[1] * Source: 2018 ILL Annual Report (page 96: numbers for panels in April 2018). The oversubscription factor of 3.6, takes into account that from the switch of IN6 to a CRG-A in October 2017, the available beam time turned to 50% of what it was previously. ** Due to the long 2017 shutdown, a large number of these 2018 experiments were backlogged. This explains why, while only 22 days have been granted to ILL users in April 2018, 60 days of ILL experiments have been performed over the whole year 2018 (see Table 1).

III. Beam time use

Table 4 shows the partition by ILL scientific college of the effective ILL and 2FDN beam-time. This statistic includes the cycle over which SHARP has welcomed users. One can notice an ILL/2FDN split of the scientific fields developed on the instrument: a very significant activity by college 7 for ILL users and a massive use by "college 6"-like experiments for 2FDN. Altogether, the college 6 and 7 are major players on the instrument (66%of the total beam-time). On can also note that the college 4 (28%) and college 7 (30%), which are very active on this instrument, will take full advantage of the Position Sensitive Detectors of SHARP^{+}.

IV. Scientific Production and Bibliometric

The annual scientific production of the instrument is almost constant to 17 papers with a large fraction of them published in high impact journals (impact factors > 10).

Over the whole 2011-2016 and 2017-2021 periods 113 and 85 papers have been respectively published. For 2017-2021, this an average of 17 papers a year. The average H-Index (32) is satisfactory. The level of citation is constantly climbing-up over the last decade.

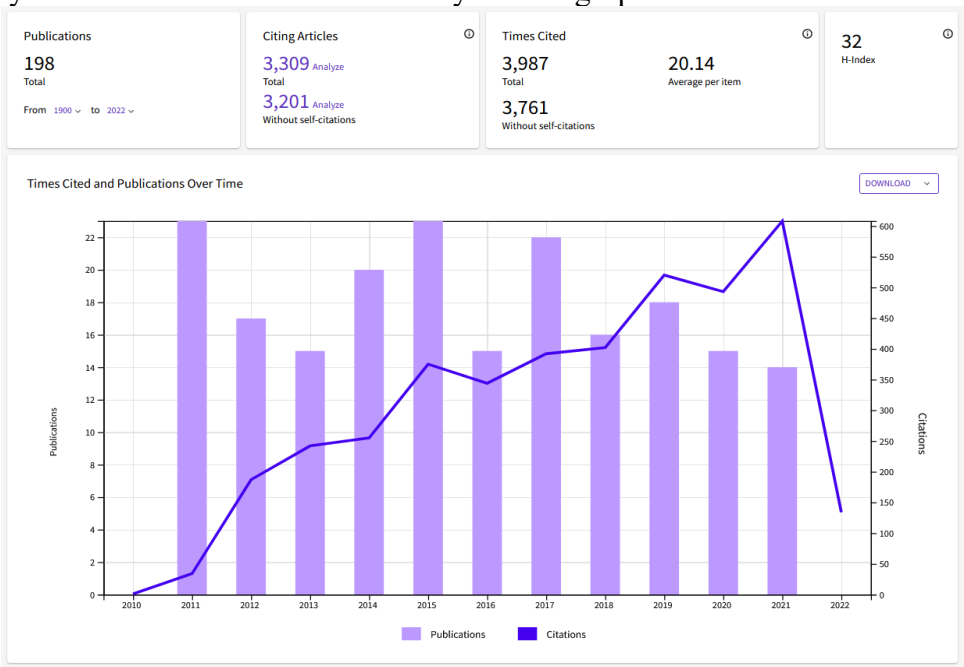

Figure 2. Bibliometric indicators of papers with data collected on IN6 (2011-2016) then on IN6-SHARP (2017-2021).

V. Instrument construction, improvements and upgrades: SHARP

SHARP Key Facts:

- IN6-SHARP has been shut-down in October 2020.
- SHARP has been constructed from November 2020 to March 2021 (Reactor cycle 189). This very short 4.5 months construction duration is a performance.
- The commissioning was done during May to Mid-July 2021 (Reactor cycle 190).
- The ToF chamber is now under excellent vacuum (10^{-3} mbar).
- The SHARP sample well (80 cm diameter) has been designed to accept all the sample environments used on IN6-SHARP.
- All the instrument materials are a-magnetic and the SHARP sample well has been designed to accept the ILL 10 T coil.
- A unique specificity of IN6 was the easy access to the sample environment by the side of the instrument and at the ground level. This capability has been maintained but extended on SHARP with a large door (**Figure 4**) giving direct access to the sample stage. Massive and complex environments can be used with spatial easy settings.
- After final tests of the radial collimator (delayed by Brexit customs related issues), official users have been welcomed for 40 days of experiments (cycle 191).
- No backlog experiments after the IN6-SHARP then SHARP operations.

General description of the instrument IN6-SHARP

IN6, then IN6-SHARP after October 2017, was a time focusing time-of-flight spectrometer designed for quasi-elastic and inelastic scattering.

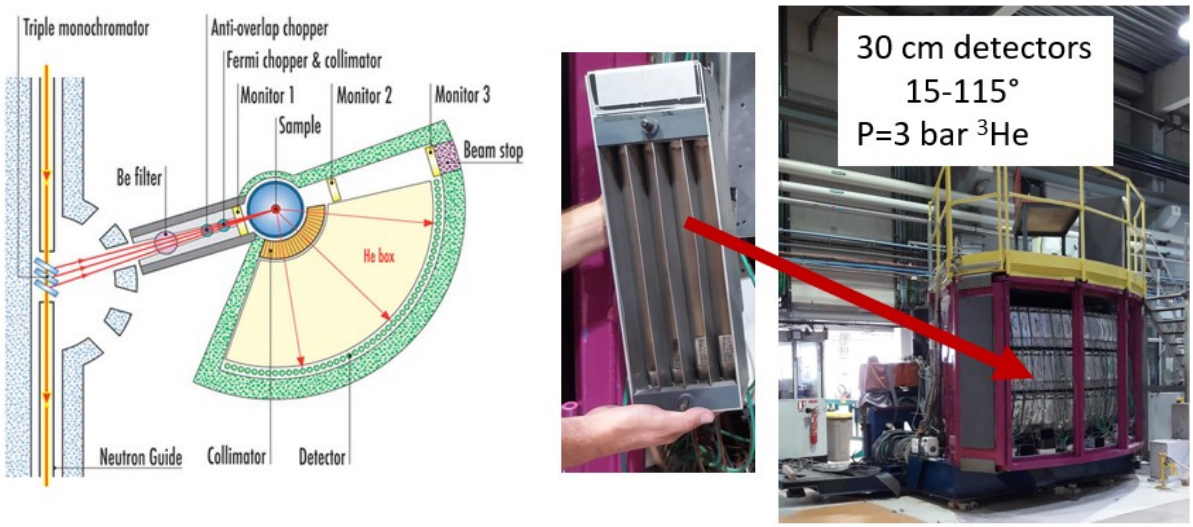

Figure 3. Left: Schematic drawing of IN6. Right: view of the IN6 detectors.

An intense beam was extracted from the H15 guide by a vertically focusing monochromator array. It was consisting of three composites 20.0*5.0 cm^2 highly oriented pyrolytic graphite (HOPG) monochromators using the full height (20 cm) of the guide to vertically focus the beam at the sample position. In order to minimize the interference with the subsequent instruments, the monochromator was delivering only four wavelengths/resolutions: 4.1 Å (170 µeV), 4.6 Å (120 µeV), 5.1 Å (70 µeV) and 5.9 Å (50 µeV). The higher order reflections from the graphite monochromator were removed by a beryllium-filter cooled at liquid nitrogen temperature.

To achieve the time-focusing condition, the beam was pulsed by a Fermi chopper. To prevent frame-overlap a Fermi suppressor chopper, operated at a lower speed, was placed before the Fermi chopper.

The secondary spectrometer was consisting first of an evacuated sample area. A helium filled box between the sample and the detectors was minimizing the background. The sample box was equipped with an oscillating collimator which prevents parasitic reflections (from the cryostat walls for example) reaching the detectors. The detector bank was entirely covered with detector boxes (equipped with 3 bar ^{3}He 337 individual detectors arranged according to the Debye-Scherrer cones to cover scattering angles from 15 to 115° (**Figure 3**).

General description of the instrument SHARP

More details here.

The SHARP (Spectromètre Hybride Alpes Région Parisienne) project has consisted in a complete rebuilding of the IN6 secondary spectrometer: sample environment, time-of-flight chamber and detection. The spectrometer has been equipped with 240 PSD (Position Sensitive Detector) under 5 bars of ^{3}He. Beyond the gain of a factor 3.7 in detection coverage solid angle, these new detectors made it possible a spectacular gain in the definition and mapping of the (Q, ω) domain.

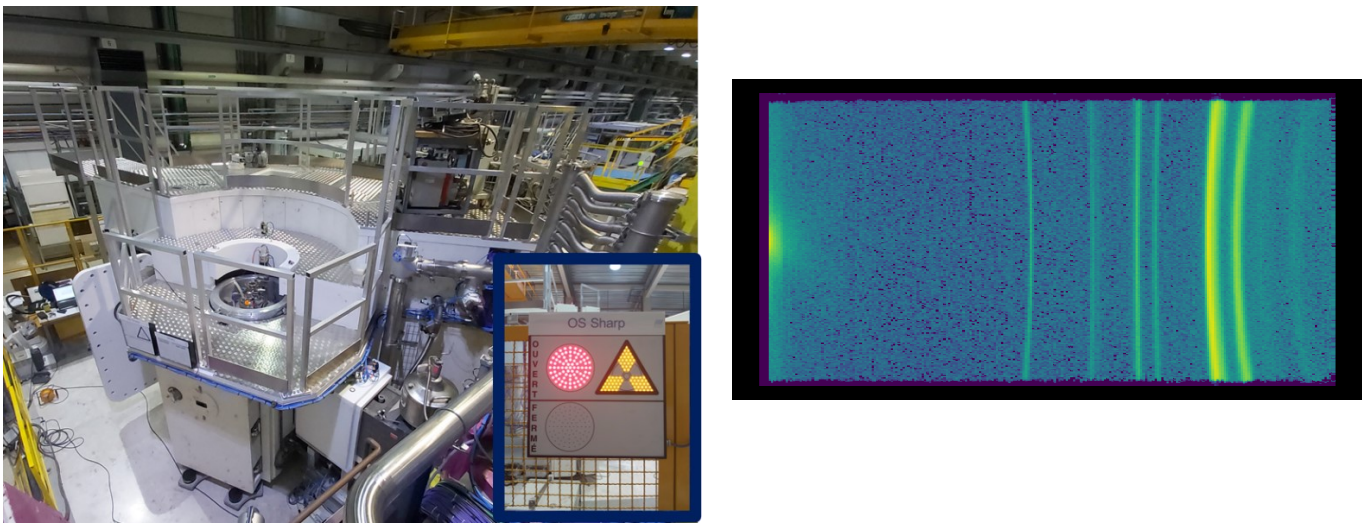

Figure 4. Left: SHARP up and running with its first neutrons: March 21 2021. Right: first spectrum measured on the 240 PSDs. The sample was deuterated Mn_{12} Acetate. Note that large door at the ground level gives direct and easy access to the sample environment stage.

The process of the Sharp construction has started right after the end of the last 2020 cycle in October and was completed on March 21 2021 when the first neutrons have enlightened the brand-new instrument (**Figure 4**).
The secondary spectrometer (all the elements downstream of the monochromator) has been reconstructed in a remarkable short time (4.5 months). A key part of the work has been the full furbishing of the chamber with Cd coverage, installation of 240 PSD along with their collimators and the associated electronics. As for the detection electronics, ILL technical teams have joined the LLB work-force for their cabling, testing and integration within the Data

Acquisition System. Also, a very efficient pumping system has been designed, funded and installed by the ILL vacuum group.

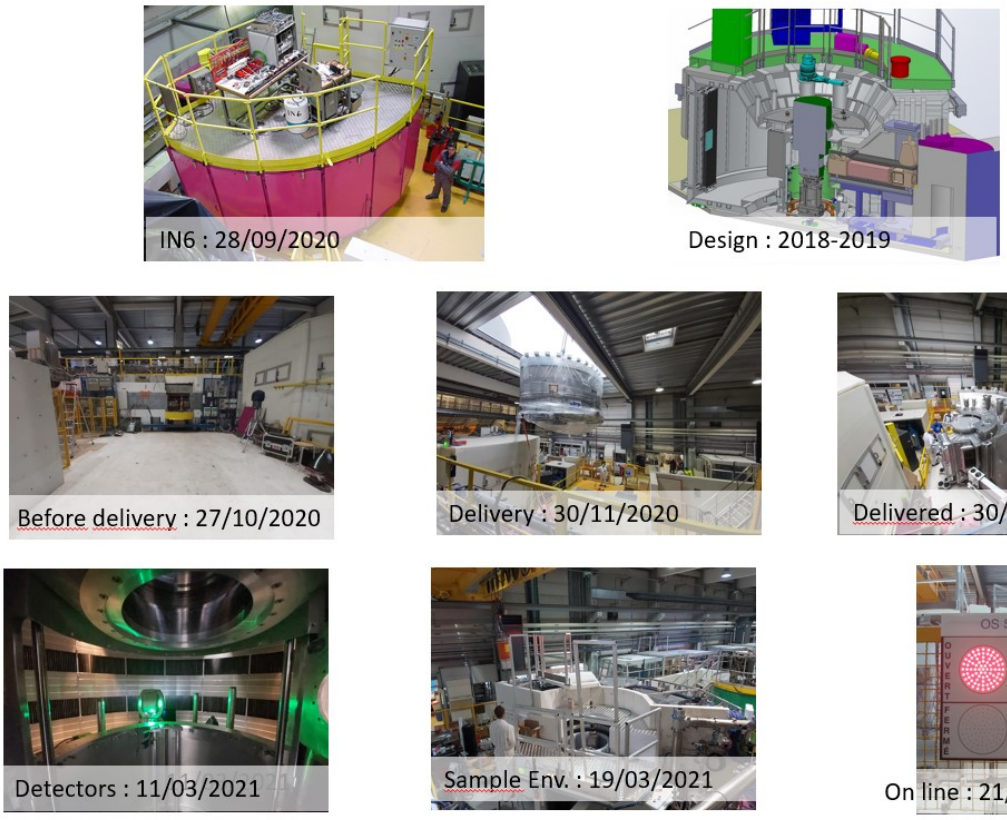

Figure 5. The key dates of the SHARP construction.

As a picture is worth a thousand words: the making-of of the construction of Sharp is shown on **Figure 5.**

The major improvement concerns the time-of-flight chamber itself. It is now under vacuum. A removable window between the sample and the inlet of the chamber enables to operate either with a sample under vacuum or under a controlled atmosphere. In the first configuration, the vacuum of the chamber also serves as the cryostat isolation vacuum. The number of windows between the sample and the detector has been minimized. This offers a very positive gain in background. The second configuration makes it possible the study of samples to be kept under controlled atmosphere or in complex environment (laser or electrical excitation for example).

VI. Instrument upgrades planned in the near future: SHARP$^+$

More details can be found here.

SHARP$^+$ Key Facts:

- SHARP$^+$ will enjoy a dedicated guide at the end of the new H15 guide.
- To save 15-20% of the flux at sample position and access wavelength below 4 Å, the IN6-SHARP Beryllium filter has been replaced by an anti-harmonics cascade of three disk choppers.
- A large (W*H=20.0*30 cm^2) HOPG (0.8° mosaïcity) monochromator will focus horizontally and vertically.
- Compared to IN6 (4.1, 4.6, 5.1, 5.9 Å), the incident wavelength range has been extended from 2 to 6 Å.
- To extend the dynamical range to the wavelength band 7 to 12 Å and reach high energy resolution (up to 30 μeV), a second monochromator with fluorinated Mica (d=9.4 Å)

is under study. See text below **Figure 9**. It is nevertheless not yet in the scope of the instrument.

- SHARP$^+$ will be a hybrid instrument offering two distinct modes: Time Focusing and Monochromatic Focusing.
- The switch from one mode to the other will be ensured by a turn-key retractable 4.5 m section of the guide.
- SHARP$^+$ will use a brand-new 400 Hz Fermi-Chopper.

A long (2021-2024) H15 guide shutdown is needed partly for the re-construction and extension of this guide. By the end of this process, the secondary spectrometer of Sharp will be moved to the end of this new guide. The instrument will then become SHARP$^+$.
SHARP$^+$ will take advantage of a guide-end position starting after the SHARP$^+$/SAM branch. The guide geometry and coverage optimize the flux at sample position. The SHARP$^+$ branch will adopt a constant radius of curvature of 2000 m. It is composed of a first straight section (W*H=6*20 cm^2) followed by a 14 m long horizontal and vertical elliptic converging section (down to W*H=3*5 cm^2). The m coverage of the straight section is moderate (m=1.5 and 2) while the coverage of the top and bottom of the converging section rises to 5. There is no direct sight and the wavelength cut-off is 1.5 Å. SHARP$^+$ is designed to operate on a large range of incident wavelength from 2 to 12 Å.

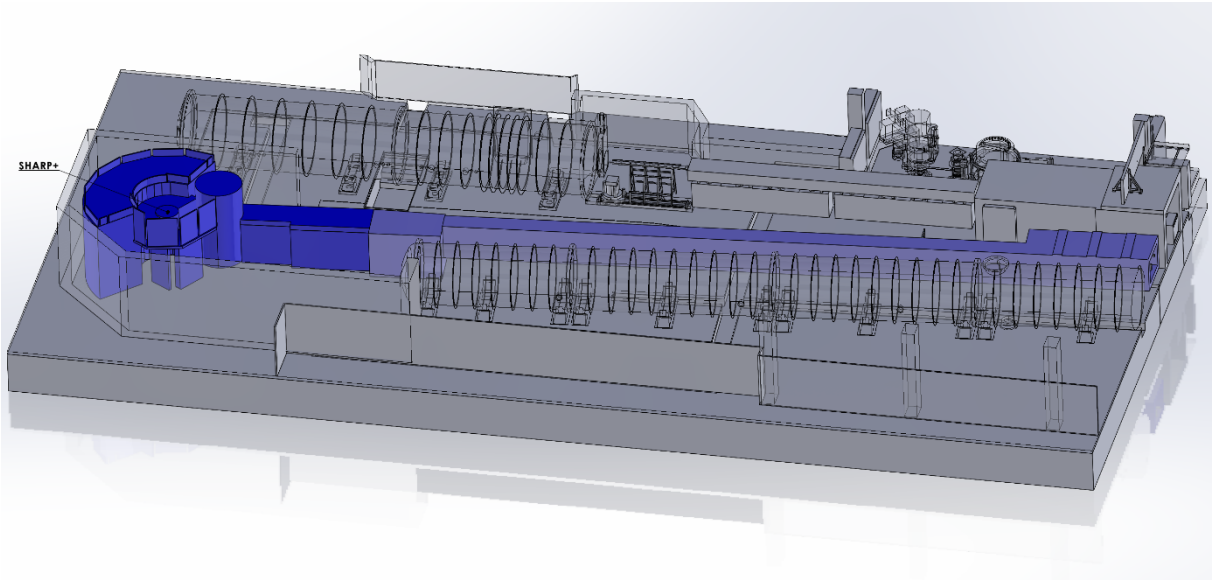

Figure 6. SHARP $^+$, in blue, at the end of the reconstructed H15 guide in between D11 and D33.

SHARP$^+$ will combine two modes: a Time Focusing (TF) mode as on IN6 and an additive so-called Monochromatic Focusing (MF) mode. TF will primarily beneficiate to quasi-elastic studies in soft matter and experiments in solid-state physics where a good resolution (few tens of μeV) is needed on a narrow range of energy transfer. The MF mode is optimized for studies requiring the same kind of resolution but on a wide range of energy transfer (mainly studies in the field of material science). The price to pay for this constant resolution is a decrease in flux compared to the Time Focusing mode.
A brand-new Fermi Chopper (FC) with maximum speed of 400 Hz will beneficiate to the two modes of the instrument. In the TF mode it will make it possible to realize inelastic TF (*i.e.* to increase resolution on a narrow range of energy transfer) as far as $\hbar w$ = 50 meV on the neutron energy gain side.
The instrument will be equipped by a W*H=20*30 cm^2 two faces horizontal and vertical focusing monochromator. On one side, PG will be used for incident wavelength from 2 to 6 Å

and on the other side could use Fluorinated Mica for wavelengths from 7 to 13 Å (under study, see below).

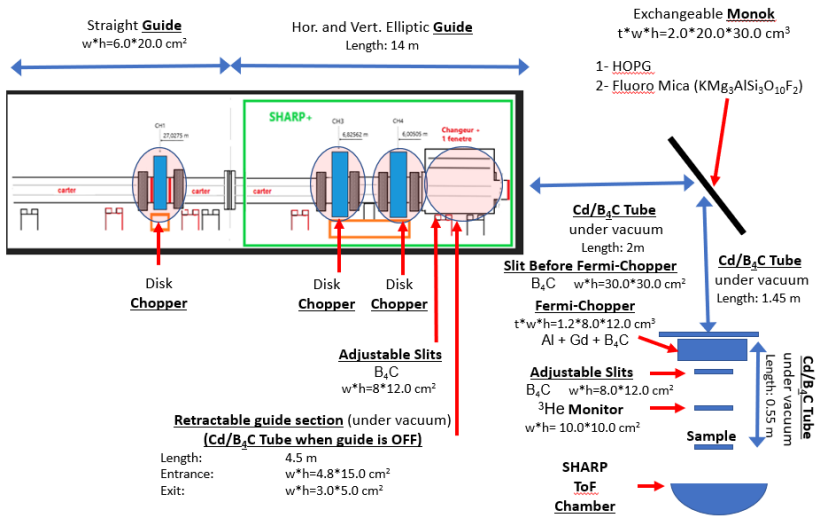

Figure 7. Schematic drawing of SHARP +, showing the key components of the instruments along with few characteristic distances. The 14 m section in green is a doubly elliptic converging section with m from 2 to 5. In order to swich from time focusing to monochromatic mode, the 4.5 m end of this guide is retractable. The three disk-choppers, with two 8.5 cm slits each, have a maximum speed of 200 Hz. This copes the maximum of the Fermi-Chopper one: 400 Hz.

The switch from the MF to the TF mode will be possible by retracting a 4.5-meter-long section at the end of the converging guide section (turn-key system *i.e.* no manpower required).

Monochromatic Focusing ("IN5 like")

λ (Å)	Sample Temp. (K)	ν_{FC} (Hz)	AO Chopper Ratio	R (μeV)	Flux @ Samp. (10^5 n/cm2/s)	Solid Angle ratio	P(^{3}He) Gain	Xtal Refectivity	$T_{Windows}$	Counting Rate (10^5 n/cm^2/s)
5	30	5	1	116	5.87	3.65	1.05	0.88	0.95	18.8
5	300	5	2	116	2.88	3.65	1.05	0.88	0.95	9.2

Time Focusing ("IN6 like")

λ (Å)	Sample Temp. (K)	ν_{FC} (Hz)	AO Chopper Ratio	R (μeV)	Flux @ Samp. (10^5 n/cm2/s)	Solid Angle ratio	P(^{3}He) Gain	Xtal Refectivity	$T_{Windows}$	Counting Rate (10^5 n/cm^2/s)
5	30	133	1	99	4.73	3.65	1.05	0.88	0.95	15.2
5	300	133	2	99	3.6	3.65	1.05	0.88	0.95	11.5
5	300	114	1	107	5.68	3.65	1.05	0.88	0.95	18.2

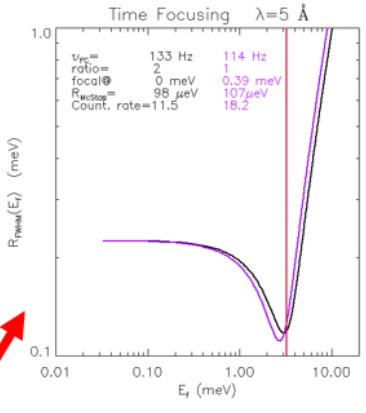

Figure 8. As a hybrid instrument, SHARP+, will offer a time focusing ("IN6-like") and a monochromatic mode ("IN5-like"). The former is designed for experiment where a high/higher resolution is needed only on a narrow energy transfer range. The latter, when a constant energy resolution is needed on an extended range. These tables, indicate the counting rate (for reference, at his best of 5.1 Å, IN6 was 10^5 n.cm^{-2}s^{-1}) and resolution as a function of operating mode and temperature. In each case, the Fermi Chopper speed (ν_{FC}) and Anti-Overlap (AO) ratio settings are indicated. For the sake of comparison, the top table shows the performances of the monochromatic mode at 5.0 Å with ν_{FC}=133 Hz i.e. the Fermi chopper frequency needed to achieve the time-focusing condition (bottom table). In this mode, compared to IN6, SHARP + is expected to offer a counting rate gain of 15±1 (McStas calculations). To avoid the ratio 2 needed to avoid frame overlap at high temperature, a slightly "off" time-focusing condition, with a decreased resolution by 10% and flux gain of 50% could be used. The resolution vs the neutron scattered energy of the perfect time-focusing condition and of the "off" one are shown on the right plot.

To be able to use incident wavelength from 2 to 4 Å (beryllium cut-off), the instrument will not be equipped with a beryllium filter (BF). This will avoid a 15-20% absorption of the beam scattered by the monochromator and will reduce the health physics protection of the instrument. Instead of using a BF, the suppression of harmonics of the nominal wavelength will be ensured by 3 disk-choppers having a maximum speed of 200 Hz. This speed with 2 slits by chopper will cope the maximum speed of the Fermi-Chopper (FC): 400 Hz. One of the disk choppers running

at an integer fraction of the FC speed will be used as anti-overlap system. The most downstream chopper will be placed just upstream of the removable guide section (**Figure 7**).
Compared to IN6, the counting rate of SHARP$^+$ is expected to be significantly above one order of magnitude (*15 in Time Focusing mode) larger and with a significantly reduced background (**Figure 8**). The commissioning is scheduled to start in April 2024.

Future possible improvement:

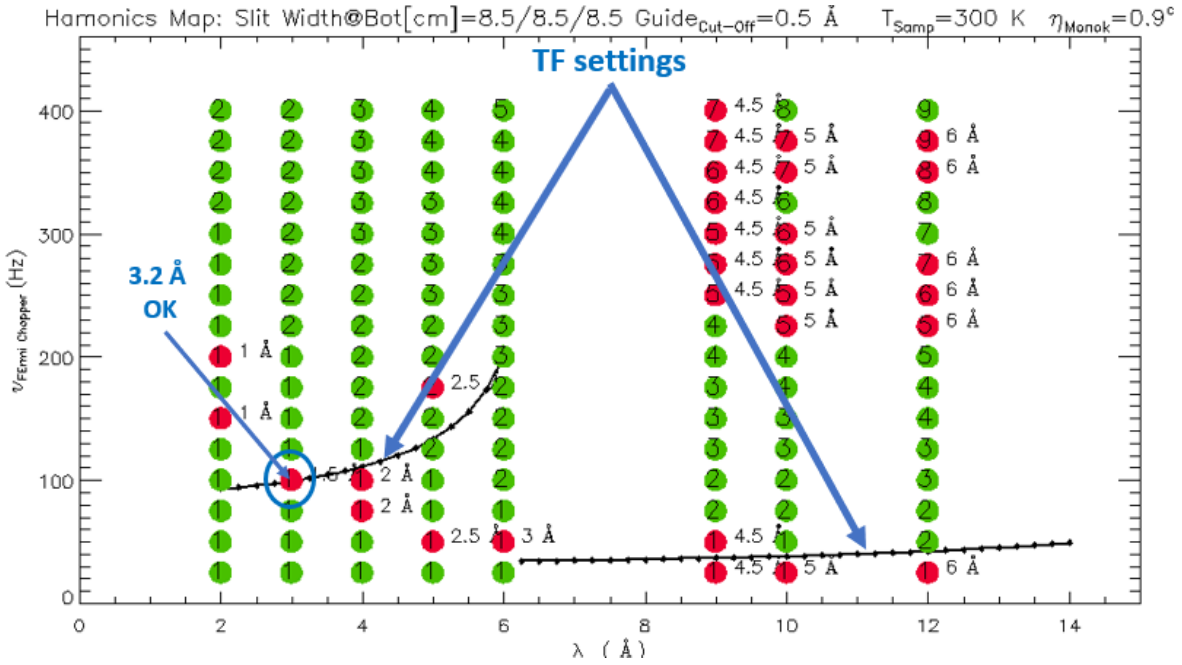

Figure 9. SHARP$^+$ [λ, $\nu_{Fermi\ chopper}$] "harmonics Map" ($\nu_{Fermi\ Chopper}$ is the Fermi Chopper frequency). For each setting, the green or red full circles indicate respectively the absence or the presence of harmonics of the nominal wavelength. The anti-overlap ratios are indicated inside each circle. In reason of a budget squeeze, following the ILL management request, one of the four foreseen anti-harmonics chopper cascade had to be suppressed. As a consequence, as harmonics will reach the sample, few settings will be "forbidden" (full red circles, the largest harmonic wavelength is indicated). The black lines are the [λ, $\nu_{Fermi\ Chopper}$] Time-Focusing condition settings. On the range 2 to 6, the time focusing condition will be possible with no harmonics. At large wavelength in the 9-12 Å range, as this leads to low chopper speed, we expect the Time-Focusing condition to be challenging to maintain. As, in the monochromatic mode, for any incident wavelength, the chopper speed can be chosen on a "Flux-Resolution" compromise basis, this is the mode that will be used for long wavelengths.

1- Additive Monochromator to reach long wavelengths for energy resolution below 50 µeV.

● **Why long wavelength?** As shown on **Table 4**, scientific issues developed by college 6 and 7 are very active on the instrument. To disentangle different dynamical contributions, these experiments very often need to use different energy resolutions. This is for example the case for liquids where rotational and translational contributions need to be measured independently. This is made possible by using a moderate resolution (100 µeV) and a much better one (30-50 µeV). This resolution range can only be achieved by using long wavelength in the 8-12 Å range.
● **Which Monochromator crystal?** While not in the scope of the instrument yet, to extend the incident wavelength range, the design makes it possible to use a second monochromator. Fluorinated Mica (d = 9.4 Å), to reach 7 to 12 Å is envisioned and currently tested with encouraging results. This material is hydrogen free so high incoherent scattering and recoil can

be avoided. Bending of the Mica sheets to increase their reflectivity will be the key to use this material. We have checked this is possible.
At 9 Å in Monochromatic mode, with $\nu_{\text{Fermi Chopper}}$=100 Hz and ratio=2, even with a very pessimistic reflectivity of Fluorinated Mica of 0.3, the counting rate for a 40 μeV resolution is expected to be equal to the one of IN6 at its best *i.e.* 5.1 Å and 70 μeV resolution. In the same conditions at 10 Å, a 30 μeV resolution can be achieved with the same counting rate of IN6 at 5.9 Å and 50 μeV resolution.

It should be noted that the SHARP$^+$ flight path (2.5 m) is significantly shorter than flight path of disk-choppers spectrometers (4.5-5 m). This will allow to use smaller anti-overlap ratios and compensate the flux loss induced by the use of a monochromator.
● **Time Focusing of Monochromatic Mode?** At long wavelengths, the time focusing condition will be challenging to achieve because a low chopper speed (40 Hz, see **Figure 9**). As in this mode, the chopper speed is a free parameter, the Monochromatic Focusing mode will lift this difficulty.

2- Additive Disk chopper to avoid instrumental settings remaining harmonics.
From the beginning of the SHARP$^+$ design, the scientific team made it clear that to fully avoid harmonics, four disk-chopper were needed. Nevertheless, due to the ILL 2019-2020 budget crisis, the ILL management asked us to propose a design with only 3 disk-choppers.
This has been possible. The technical performance counterpart is that in few instrumental conditions harmonics are not fully eliminated. These settings therefore become "Forbidden". This difficulty could be lifted by installing a fourth disk-chopper 0.5-1 m upstream of the first one. With this additive chopper, it will be possible to relax the condition of the disk-choppers slit width to go from 8.5 to 11.5 cm. This would eliminate all "harmonics forbidden settings" and, more importantly, improve the flux at sample by 30%.

VII. Technical problems

The main concern over the five years has been the two Fermi-Choppers electronics. This was a design of the nineties and spare parts/maintenance are not possible anymore. SHARP$^+$, will enjoy a brand-new Fermi chopper.
Due to a "tired mechanical system" we have experienced numerous secondary shutter failures. Altogether, the primary spectrometer of IN6-SHARP (then SHARP) was at the end of its life. This issue is solved as the primary spectrometer of SHARP$^+$ will be fully renewed.

VIII. Relations with ILL services

As a type "A" CRG, IN6-SHARP is considered as a full ILL instrument for sample environment and maintenance. On the day-to-day basis, we interact with SANE, the Services For Advanced Neutron Environments and the IT group for Data Acquisition System issues. The relationships with all the ILL services are excellent.

Figure 10. SDMS (the French boiler-maker and welding company that made ToF chamber), LLB and ILL actors of the construction of SHARP. For better readability, an enlarged version of the right part is given in Annex 2.

It should be noticed that ILL has taken active part in the construction of SHARP for the testing of the detectors (full last generation Electronics) and designing the installing the ToF chamber vacuum system.
The availability of the Health Physics group could be improved, as one to two days by cycle are lost in waiting for clearance or during radiation survey for instrument security files.

IX. Training program

Schools

IN6-SHARP has participated to the doctoral and post-doctoral formation through the HERCULES school. It includes a five-week course designed to provide training for students, postdoctoral and senior scientists from European and non-European universities and laboratories, in the field of Neutron and Synchrotron Radiation for condensed matter studies (Biology, Chemistry, Physics, Materials Science, Geosciences and Industrial applications). Lectures, practicals and tutorials, visits of Large Facilities and a poster session are proposed by the school. IN6-SHARP has received several groups of 4 students each, for practical and data analysis.

Figure 11. A group of FANs du LLB students on the SHARP platform (October 11-12 2021).

The Laboratoire Léon Brillouin is yearly organizing, an "Annual Neutronics Training" (FAN: Formation à la diffusion Neutronique) for researchers wishing to learn or become familiar with the neutron scattering techniques and experimental methods for condensed matter studies. SHARP has received several groups of LLB FANs (**Figure 11**).

PhD and Postdocs:

On IN6-SHARP, the experimental teams of almost all visitors are composed of a PhD student and/or a postdoc.

On the time range 2018-2021, 8 PhD students have defended their PhD by using IN6-SHARP data (see publication lists).

X. Scientific highlights – Abstracts

YEAR 2018

This is an open access article published under a Creative Commons Attribution (CC-BY) License, which permits unrestricted use, distribution and reproduction in any medium, provided the author and source are cited.

CHEMISTRY OF MATERIALS
Cite This: Chem. Mater. XXXX, XXX, XXX–XXX
Article
pubs.acs.org/cm

Brownmillerite-Type Sr_2ScGaO_5 Oxide Ion Conductor: Local Structure, Phase Transition, and Dynamics

Chloe A. Fuller,[†] Quentin Berrod,[‡] Bernhard Frick,[§] Mark R. Johnson,[§] Stewart J. Clark,[∥] John S. O. Evans,*[,†] and Ivana Radosavljevic Evans*[,†]

[†]Department of Chemistry, Durham University, Science Site, South Road, Durham DH1 3LE, United Kingdom
[‡]CNRS-CEA-Université Grenoble Alpe SyMMES, 38000 Grenoble, France
[§]Institut Laue Langevin, 71 Rue de Martyrs, 38000 Grenoble, France
[∥]Department of Physics, Durham University, Science Site, South Road, Durham DH1 3LE, United Kingdom

Supporting Information

ABSTRACT: Brownmillerite-type Sr_2ScGaO_5 has been investigated by a range of experimental X-ray and neutron scattering techniques (diffraction, total scattering, and spectroscopy) and density functional theory calculations in order to characterize its structure and dynamics. The material undergoes a second-order phase transition on heating during which a rearrangement of the $(GaO_{4/2})_\infty$ tetrahedral chains occurs, such that they change from being essentially fully ordered in a polar structure at room temperature to being orientationally disordered above 400 °C. Pair distribution function analysis carried out using neutron total scattering data suggests that GaO_4 tetrahedra remain as fairly rigid units above and below this transition, whereas coordination polyhedra in the $(ScO_{6/2})_\infty$ layers distort more. Inelastic neutron scattering and phonon calculations reveal the particular modes that are associated with this structural change, which may assist ionic conductivity in the material at higher temperatures. On the basis of the correlations between these findings and the measured conductivity, we have synthesized a derivative compound with increased conductivity and suggest a possible conduction mechanism in these brownmillerite-type solid electrolytes.

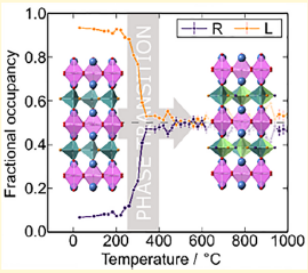

YEAR 2019

This is an open access article published under a Creative Commons Attribution (CC-BY) License, which permits unrestricted use, distribution and reproduction in any medium, provided the author and source are cited.

JACS JOURNAL OF THE AMERICAN CHEMICAL SOCIETY

Article

Cite This: J. Am. Chem. Soc. 2019, 141, 9989−9997

pubs.acs.org/JACS

Insight into Design of Improved Oxide Ion Conductors: Dynamics and Conduction Mechanisms in the $Bi_{0.913}V_{0.087}O_{1.587}$ Solid Electrolyte

Joseph R. Peet,[†,‡] Chloe A. Fuller,[†,‡] Bernhard Frick,[‡] Michael M. Koza,[‡] Mark R. Johnson,[‡] Andrea Piovano,[*,‡] and Ivana Radosavljevic Evans[*,†]

[†]Department of Chemistry, Durham University, Science Site, South Road, Durham, DH1 3LE, United Kingdom

[‡]Institut Laue Langevin, 71 Avenue des Martyrs, 38000 Grenoble, France

Supporting Information

ABSTRACT: Extensive quasielastic neutron scattering measurements have been used to directly observe oxide ion dynamics on the nanosecond time scale in bismuth vanadate with formula $Bi_{0.913}V_{0.087}O_{1.587}$, which exhibits remarkable oxide ion conductivity at low temperatures. This is the longest time scale neutron scattering study of any fluorite-type solid electrolyte, and it represents only the second case of oxide ion dynamics in any material observed on a nanosecond time scale by quasielastic neutron scattering. Ab initio molecular dynamics simulations reveal two mechanisms that contribute to the oxide ion dynamics in the material: a slower diffusion process through the Bi−O sublattice and a faster process which corresponds to more localized dynamics of the oxide ions within the VO_x coordination spheres. The length of the trajectories simulated and the validation of the simulations by neutron scattering experiments provide for the first time a quantitative insight into the relative contributions of the two processes to the oxide ion conduction in this exceptional solid electrolyte, which can be used to derive design principles for the preparation of related oxide ion conductors with even better properties.

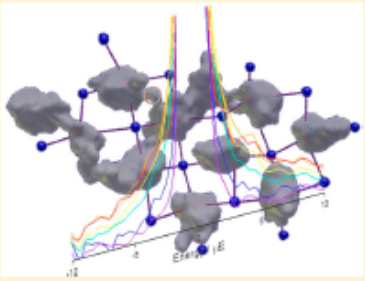

YEAR 2020

JACS
JOURNAL OF THE AMERICAN CHEMICAL SOCIETY
pubs.acs.org/JACS Article

Under Pressure: Mechanochemical Effects on Structure and Ion Conduction in the Sodium-Ion Solid Electrolyte Na_3PS_4

Theodosios Famprikis,* Ö. Ulaş Kudu, James A. Dawson, Pieremanuele Canepa, François Fauth, Emmanuelle Suard, Mohamed Zbiri, Damien Dambournet, Olaf J. Borkiewicz, Houssny Bouyanfif, Steffen P. Emge, Sorina Cretu, Jean-Noël Chotard, Clare P. Grey, Wolfgang G. Zeier, M. Saiful Islam,* and Christian Masquelier*

Cite This: *J. Am. Chem. Soc.* 2020, 142, 18422−18436 Read Online

ACCESS | Metrics & More | Article Recommendations | Supporting Information

ABSTRACT: Fast-ion conductors are critical to the development of solid-state batteries. The effects of mechanochemical synthesis that lead to increased ionic conductivity in an archetypical sodium-ion conductor Na_3PS_4 are not fully understood. We present here a comprehensive analysis based on diffraction (Bragg and pair distribution function), spectroscopy (impedance, Raman, NMR and INS), and *ab initio* simulations aimed at elucidating the synthesis−property relationships in Na_3PS_4. We consolidate previously reported interpretations regarding the local structure of ball-milled samples, underlining the sodium disorder and showing that a local tetragonal framework more accurately describes the structure than the originally proposed cubic one. Through variable-pressure impedance spectroscopy measurements, we report for the first time the activation volume for Na^+ migration in Na_3PS_4, which is ~30% higher for the ball-milled samples. Moreover, we show that the effect of ball-milling on increasing the ionic conductivity of Na_3PS_4 to $\sim 10^{-4}$ S/cm can be reproduced by applying external pressure on a sample from conventional high-temperature ceramic synthesis. We conclude that the key effects of mechanochemical synthesis on the properties of solid electrolytes can be analyzed and understood in terms of pressure, strain, and activation volume.

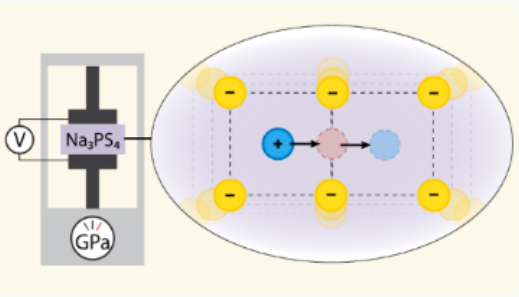

YEAR 2021

nature COMMUNICATIONS

ARTICLE

https://doi.org/10.1038/s41467-021-22182-4 OPEN

Diffusion in dense supercritical methane from quasi-elastic neutron scattering measurements

Umbertoluca Ranieri[1,2✉], Stefan Klotz[3], Richard Gaal[4], Michael Marek Koza[2] & Livia E. Bove[3,5✉]

Methane, the principal component of natural gas, is an important energy source and raw material for chemical reactions. It also plays a significant role in planetary physics, being one of the major constituents of giant planets. Here, we report measurements of the molecular self-diffusion coefficient of dense supercritical CH_4 reaching the freezing pressure. We find that the high-pressure behaviour of the self-diffusion coefficient measured by quasi-elastic neutron scattering at 300 K departs from that expected for a dense fluid of hard spheres and suggests a density-dependent molecular diameter. Breakdown of the Stokes–Einstein–Sutherland relation is observed and the experimental results suggest the existence of another scaling between self-diffusion coefficient D and shear viscosity η, in such a way that $D\eta/\rho$=constant at constant temperature, with ρ the density. These findings underpin the lack of a simple model for dense fluids including the pressure dependence of their transport properties.

[1] Center for High Pressure Science & Technology Advanced Research (HPSTAR), Shanghai, China. [2] Institut Laue-Langevin, Grenoble Cedex 9, France. [3] Sorbonne Université, UMR CNRS 7590, Institut de Minéralogie, de Physique des Matériaux et de Cosmochimie (IMPMC), Paris, France. [4] Laboratory of Quantum Magnetism (LQM), École Polytechnique Fédérale de Lausanne, Lausanne, Switzerland. [5] Dipartimento di Fisica, Universitá di Roma La Sapienza, Roma, Italy. ✉email: umbertoluca.ranieri@hpstar.ac.cn; liviaeleonora.bove@uniroma1.it

YEAR 2022
(January to June)

nature materials

ARTICLES

https://doi.org/10.1038/s41563-022-01197-2

Check for updates

Disentangling water, ion and polymer dynamics in an anion exchange membrane

Fabrizia Foglia[1]✉, Quentin Berrod[2], Adam J. Clancy[1], Keenan Smith[3], Gérard Gebel[2], Victoria García Sakai[4], Markus Appel[5], Jean-Marc Zanotti[6], Madhusudan Tyagi[7,8], Najet Mahmoudi[4], Thomas S. Miller[3], John R. Varcoe[9], Arun Prakash Periasamy[9], Daniel J. L. Brett[3], Paul R. Shearing[3], Sandrine Lyonnard[2]✉ and Paul F. McMillan[1,10]

Semipermeable polymeric anion exchange membranes are essential for separation, filtration and energy conversion technologies including reverse electrodialysis systems that produce energy from salinity gradients, fuel cells to generate electrical power from the electrochemical reaction between hydrogen and oxygen, and water electrolyser systems that provide H_2 fuel. Anion exchange membrane fuel cells and anion exchange membrane water electrolysers rely on the membrane to transport OH^- ions between the cathode and anode in a process that involves cooperative interactions with H_2O molecules and polymer dynamics. Understanding and controlling the interactions between the relaxation and diffusional processes pose a main scientific and critical membrane design challenge. Here quasi-elastic neutron scattering is applied over a wide range of timescales (10^0–10^3 ps) to disentangle the water, polymer relaxation and OH^- diffusional dynamics in commercially available anion exchange membranes (Fumatech FAD-55) designed for selective anion transport across different technology platforms, using the concept of serial decoupling of relaxation and diffusional processes to analyse the data. Preliminary data are also reported for a laboratory-prepared anion exchange membrane especially designed for fuel cell applications.

[1]Department of Chemistry, Christopher Ingold Laboratory, University College London, London, UK. [2]Université Grenoble Alpes, CNRS, CEA, IRIG-SyMMES, Grenoble, France. [3]Electrochemical Innovation Lab, Department of Chemical Engineering, University College London, London, UK. [4]ISIS Neutron and Muon Source, Science & Technology Facilities Council, Rutherford Appleton Laboratory, Harwell Science and Innovation Campus, Chilton, UK. [5]Institut Laue Langevin, Grenoble, France. [6]Laboratoire Léon Brillouin (CEA-CNRS), Université Paris-Saclay, CEA Saclay, Gif-sur-Yvette Cedex, France. [7]NIST Center for Neutron Research (NCNR), National Institute of Standards and Technology, Gaithersburg, MD, USA. [8]Department of Materials Science and Engineering, University of Maryland, College Park, MD, USA. [9]Department of Chemistry, University of Surrey, Guildford, UK. [10]Deceased: Paul F. McMillan.
✉e-mail: f.foglia@ucl.ac.uk; sandrine.lyonnard@cea.fr

XI. List of experiments

Cycle 182

Proposal #	First applicant	Title	# of days	Schedule dates	CRG/ILL	Local Contact
CRG-2483	J.-M. Zanotti, LABORATOIRE LEON BRILLOUIN, Saclay, France	Ionic Liquid under 1D nanometric confinement in CNT membranes: gigantic transport properties?	7	08/03/2018-15/03/2018	CRG	J.-M. Zanotti
7-01-456	M. MURSHED, INST INORG & PHYS CHEM, BREMEN, Germany	Phonon density of states of PbFeBO4, PbMnBO4, and PbFe0.5Mn0.5BO4 studied by inelastic neutron scattering	4	15/03/2018-19/03/2018	ILL	M. Koza
7-01-465	M. BEAUDHUIN, UNIV. MONTPELLIER, France	Effect of the dimensionality on the lattice dynamics and anharmonicity of thermoelectric silicides	7	19/03/2018-26/03/2018	ILL	M. Koza
TEST-2805	Hercules	Practical Solid-State Physics	1	26/03/2018-27/03/2018	ILL	S. Petit, L. Mangin-Thro
TEST-2806	Hercules	Practicals Soft Matter	1	27/03/2018-28/03/2018	CRG	Q. Berrod, J.-M. Zanotti
7-05-476	A. TAMTOEGL, CAVENDISH LAB., CAMBRIDGE, UK	The role of inter-adsorbate interactions and adsorption geometry in surface diffusion	5	28/03/2018-02/04/2018	ILL	M. Koza
4-04-492	E. KERMARREC, CNRS/LABORATOIRE DE PHYSIQUE DES SOLIDES, ORSAY, France	Spin dynamics and anisotropy of a new quantum pyrochlore magnet	2	04/04/2018-06/04/2018	ILL	B. Fak
4-04-494	D. ADROJA, RUTHERFORD APPLETON LABORATORY, DIDCOT, UK	Inelastic Neutron Scattering study on heavy fermion oxypnictide Ce(Ru1-xFex)PO	3	06/04/2018-09/04/2018	ILL	B. Fak
TEST-2840	M. ZBIRI, ILL, GRENOBLE	Dynamics and Anamalous Expansion in A2M3O12	2	09/04/2018-11/04/2018	ILL	M. Zbiri

6-07-26	A. GUILBERT, IMPERIAL COLLEGE, London, UK	Probing the vibrational and local dynamics of conjugated microporous materials for photocatalysis applications	5	11/04/2018-16/04/2018	ILL	M. Zbiri
7-03-167	R. SEVCIK, CENTRE OF EXCELLENCE, TELC, CZECH REPUBLIC	Investigation of the crystallization reaction of calcium carbonate from amorphous precursor with quasielastic neutron scattering	2	16/04/2018-18/04/2018	ILL	M. Zbiri
CRG-2486	P. JUDEINSTEIN, LABORATOIRE LEON BRILLOUIN, Saclay, France	Structure and dynamics of the hydro gen-bond network in water crystallization arrays	5	20/04/2018-25/04/2018	CRG	J.-M. Zanotti, Q. Berrod

Cycle 183

Proposal #	First applicant	Title	# of days	Schedule dates	CRG/ILL	Local Contact
CRG-2504	S. LYONNARD, CEA GRENOBLE INAC/SI3M/PCI,Grenoble, France	Ion dynamics in Thermotropic Ionic Liquid Crystalline Polymers	6	22/05/2018-28/05/2018	CRG	J.-M. Zanotti, Q. Berrod
CRG-2503	L. CHAIX, CNRS, GRENOBLE, France	Inelastic neutron scattering study of dynamical properties of Fe2.5Mn0 .5BO5 and Fe1.75Mn1.25BO5 ludwigite s	7	28/05/2018-04/06/2018	CRG	Q. Berrod, S. Petit
CRG-2516	E. LHOTEL Elsa : CNRS/INSTITUT NEEL, GRENOBLE, France	Low energy magnetic ex citations in Tb2Ir2O7	3	04/06/2018-07/06/2018	CRG	Q. Berrod, S.Petit
CRG-2515	C. COLIN, LABORATOIRE LEON BRILLOUIN, Saclay, France	Investigation of the hy steric hybrid improper ferroelectric transition in NaLaCoWO6	4	07/06/2018-11/06/2018	CRG	S. Petit
CRG-2514	E. LHOTEL, CNRS/INSTITUT NEEL, GRENOBLE, France	Low energy excitations in Er2Ir2O7	4	11/06/2018-15/06/2018	CRG	Q. Berrod, S. Petit
CRG-2505	CHABOUSSANT Gregory : LABORATOIRE LEON	Zero-field Splitting terms in the dinuclear Fe(II)	5	15/06/2018-20/06/2018	CRG	J.-M. Zanotti,

	BRILLOUIN,Saclay, France	molecular compounds				Q. Berrod
CRG-2506	U. RANIERI, ILL, GRENOBLE	Pressure effect on the quantum rotations of encaged methane	5	20/06/2018-25/06/2018	CRG	M. Koza
46940	M. MACCARINI, TIMC-IMAG, UJF ,LA TRONCHE, France	Coherent dynamics of water under hydrophobic quasi 1D confinement	2	25/06/2018-27/06/2018	ILL	M. Koza
7-03-167	R. SEVCIK, CENTRE OF EXCELLENCE, TELC, CZECH REPUBLIC	Investigation of the crystallization reaction of calcium carbonate from amorphous precursor with quasielastic neutron scattering	2	27/06/2018-29/06/2018	ILL	M. Zbiri
CRG-2534	R. VIENNOIS, INSTITUT CHARLES GERHARDT MONTPELLIER, France	Lattice dynamics of Ba24Ge100	4	29/06/2018-03/07/2018	CRG	M. Koza
TEST-2937	A. WILDES, ILL, GRENOBLE	Measuring the energy dependence of the D7 analysers	1	03/07/2018-04/07/2018	ILL	J.-M. Zanotti

Cycle 184

Proposal #	First applicant	Title	# of days	Schedule dates	CRG/ILL	Local Contact
4-05-718	E. KERMARREC, CNRS/LABORATOIRE DE PHYSIQUE DES SOLIDES, ORSAY, France	Investigation of Kagome spin dynamics on a S=1 candidate spin-liquid material Li9V3P8O29	3	07/09/2018-10/09/2018	ILL	B. Fak
CRG-2567	PETIT Sylvain : LABORATOIRE LEON BRILLOUIN, Saclay, France	Vers l'utilisation du spectrometre temps de vol IN6-Sharp en mode mono cristaux	3	10/09/2018-13/09/2018	CRG	J.-M. Zanotti
7-03-169	M. KARLSSON, CHALMERS UNIVERSITY OF TECHNOLOGY, GÖTEBORG, Sweden	Dynamics of the formamidinium organ ic cation in mixed hybrid inorganic -organic perovskites	5	13/09/2018-18/09/2018	ILL	M. Koza
CRG-2549	E. GUILMEAU, CNRS/CRISMAT, CAEN, France	Inelastic neutron scattering study of the lattice dynamics of coulusite	3	18/09/2018-21/09/2018	CRG	J.-M. Zanotti
CRG-2548	M. PLAZANET, CNRS/LIPHY, SAINT MARTIN D HERES, France	Transport of water in soft confinement	3	21/09/2018-24/09/2018	CRG	J.-M. Zanotti

CRG-2526	A. BELIME, LLB, Saclay, France	Dynamics of a Polymer Electrolyte i n bulk and under 1D CNT nanometric confinement	7	24/09/2018-01/10/2018	CRG	Q. Berrod, J.-M. Zanotti
7-01-471	S. D'AMBRUMENIL, GRENOBLE, France	Tuning phonon dynamics in the novel anomalous thermal expansion candidates, tertiary mixed-metal cyanides CuxAgyAu1-x-yCN	4	01/10/2018-05/10/2018	ILL	M. Zbiri
7-03-171	I. EVANS, UNIV DURHAM , UK	New brownmillerite-based oxide ion conductors: Direct observation of multi-scale oxide ion dynamics	5	05/10/2018-10/10/2018	ILL	Q. Berrod
7-04-165	D. PONTIROLI, UNIV PARMA, Italy	Neutron spectroscopy investigation of synthesized melanophlogite	2	12/10/2018-14/10/2018	ILL	S. Rols
CRG-2550	C. METAIS, UNIVERSITE E DE BORDEAUX, France	Transport properties of gaseous species within artificial Co2-H2 hydrate bearings	1	17/10/2018-18/10/2018,	CRG	J.-M. Zanotti
7-04-165 *Continued due to Reactor shuddown*	D. PONTIROLI, UNIV PARMA, Italy	Neutron spectroscopy investigation of synthesized melanophlogite	1	18/10/2018-19/10/2018	ILL	S. Rols
7-04-153	A. GUILBERT, IMPERIAL COLLEGE, UK	Probing dynamics in organic photovoltaics under light excitation	4	19/10/2018-23/10/2018	ILL	M. Zbiri
6-02-587	H. HANSEN, ROSKILDE UNIVERSITY, Denmark	Contribution of intramolecular moti ons to the global molecular dynamic s of cumene	1	23/10/2018-24/10/2018	ILL	B. Frick, Q. Berrod
4-05-706	Y. SU, FORSCHUNGSZENTRUM JUELICH, Germany	Inelastic neutron scattering study on the spin dynamics of potential s pin liquid Ba3LaCuReWO12	1	24/10/2018-25/10/2018	ILL	J.-M. Zanotti

CRG-2550 *Continued due to Reactor shuddown*	C. METAIS, UNIVERSITE DE BORDEAUX, France	Transport properties of gaseous species within artificial Co2-H2 hydrate bearings	3	25/10/2018-28/10/2018	CRG	J.-M. Zanotti

Proposal	Main Proposer	Title	# of Days	Schedule dates	Local Contact
		Cycle 185			
CRG-2613	**MORINEAU Denis**: IPR - UNIV RENNES 1	Dynamics of Binary Liquids in Mesopores with Periodically AlternatingSurface Interaction	7	17/06/2019-24/06/2019	J.-M. Zanotti
CRG-2616	**PETIT Sylvain**: CNCE/LLB-LAB LEON BRILLOUIN, SACLAY ,GIF-SUR-YVETTE	Vers l'utilisation du spectrom_etre temps de vol IN6-Sharp en mode monocristaux	2	24/06/2019-26/06/2019	J.-M. Zanotti
7-01-486	**MURSHED Mohammad Mangir**: INST INORG & PHYS CHEM, BREMEN	Phonon density of states of the magnetic phases from the non-magneticstructural analogues	2	26/06/2019-28/06/2019	M. Koza
CRG-2608	**BALEDENT Victor**: CNRS/LABORATOIRE DE PHYSIQUE DES SOLIDES (LPS), ORSAY	Electromagnon in GdMn2O5	3	28/06/2019-01/07/2019	J.-M. Zanotti
7-01-493	**TURNER Shelby**: ILL, GRENOBLE	Phonon dynamics in High Entropy Alloys	1	01/07/2019-02/07/2019	J.-M. Zanotti
CRG-2610	**DE BOISSIEU Marc**: CNRS/SIMAP - INPG ,SAINT MARTIN D'HERES	Dispersion relation and phonon lifetime of the Rb2ZnCl4 incommensurately modulated phase (970)	3	02/07/2019-05/07/2019	J.-M. Zanotti
9-11-1898	**GUILBERT Anne**: IMPERIAL COLLEGE LONDON, SOUTH KEN CAMPUS	Dynamical study of organic photovoltaics: extending the study from the ps to the ns timescale and investigating effect of composition	4	05/07/2019-09/07/2019	M. Zbiri
CRG-2662	**JUDEINSTEIN Patrick**: CNCE/LLB-LAB LEON BRILLOUIN, SACLAY ,GIF-SUR-YVETTE	Structure and dynamics of the hydrogen-bond network in water crystallization arrays	3	09/07/2019-12/07/2019	J.-M. Zanotti Q. Berrod
7-03-179	**FAMPRIKIS Theodosios**: LRCS-UPJV, AMIENS	Lattice Dynamics and Ion Migrationin Na3PS4 for solid state sodium batteries.	3	12/07/2019-15/07/2019	M. Zbiri

6-03-444	**BROWN Katherine**: SCHOOL OF PHYSICS & ASTRONOMY, UNIV EDINBURGH	The dynamic behaviour of CH4-H2O solutions	4	15/07/2019-19/07/2019	J.-M. Zanotti
4-05-730	**KERMARREC Edwin**: CNRS/LABORATOIRE DE PHYSIQUE DES SOLIDES (LPS), ORSAY	Spin excitations in new quantum kagome compounds of the atacamite family	4	19/07/2019-23/07/2019	J.-M. Zanotti
CRG-2615	**CHABOUSSANT Gregory**: CNCE/LLB-LAB LEON BRILLOUIN, SACLAY ,GIF-SUR-YVETTE	Search for spin waves excitations in ferromagnetic metallic nanowires	7	23/07/2019-30/07/2019	Q. Berrod J.-M. Zanotti
CRG-2636	**KERMARREC Edwin**: CNRS/LABORATOIRE DE PHYSIQUE DES SOLIDES (LPS), ORSAY	Low energy excitations of Seff=1/2traingular rare-earth based antiferromagnets	5	30/07/2019-04/08/2019	J.-M. Zanotti
		Cycle 186			
9-11-1916	**FOGLIA Fabrizia**: DEPT PHARMACY, KING'S COLLEGE LONDON	OH- and water dynamics in Anionic Exchange Membranes (AEMs)	5	30/08/2019-04/09/2019	J.-M. Zanotti Q. Berrod
CRG-2679	**TEIXEIRA Jose**: CNCE/LLB-LAB LEON BRILLOUIN, SACLAY ,GIF-SUR-YVETTE	Dynamics of water highly confined in imogolite	2	04/09/2019-06/09/2019	J.-M. Zanotti
7-05-508	**TAMTOEGL Anton**: INST. FUR EXPERIMENTALPHYSIK TU GRAZ	How does tuning the van der Waals bonding strength affect adsorbate structure and nanoscale diffusion?	3	06/09/2019-09/09/2019	M. Koza
6-07-48	**GUILBERT Anne**: IMPERIAL COLLEGE LONDON, SOUTH KEN CAMPUS	Probing the vibrational and local dynamics of conjugated microporous materials for photocatalysis applications	3	09/09/2019-12/09/2019	M. Zbiri
7-04-168	**GUILBERT Anne**: IMPERIAL COLLEGE LONDON, SOUTH KEN CAMPUS	Structural dynamics of bulk heterojunction with non-fullerene acceptors for organic photovoltaics	2	12/09/2019-14/09/2019	M. Zbiri
7-01-489	**D'AMBRUMENIL Stella**: ILL, GRENOBLE	Negative Thermal Expansion in isotopically substituted Cd(CN)2 and its precursor Cd(NH3)2[Cd(CN)4]	3	14/09/2019-17/09/2019	M. Zbiri

CRG-2678	**LHOTEL Elsa**: CNRS GRENOBLE - INSTITUT NEEL	Low energy magnetic excitations inNd2Ir2O7, a candidate for magneticfragmentation	3	17/09/2019-20/09/2019	Q. Berrod
CRG-2671	**PETIT Sylvain**: CNCE/LLB-LAB LEON BRILLOUIN, SACLAY ,GIF-SUR-YVETTE	Spin dynamics in rare earth garnets	3	20/09/2019-23/09/2019	Q. Berrod
CRG-2676	**GRENIER Beatrice**: UFR PHITEM, GRENOBLE, SAINT-MARTIN-D'HÈRES	Inelastic neutron scattering studyof a neary isolated s=1/2 triangular system KBa3Ca4Cu3V7O28	3	23/09/2019-26/09/2019	S. Petit Q. Berrod
CRG-2677	**GOBAUT Benoit**: LABORATOIRE LÉON BRILLOUIN UMR12 CEA-CNRS	Studying the ZFS terms in photoswitchable Prussian Blue Analog nanoparticles	4	26/09/2019-30/09/2019	J.-M. Zanotti Q. Berrod
CRG-2607	**GIORDANO Valentina**: ILM - UCBL 1, VILLEURBANNE	Temperature dependence of phonon dynamics in a Eutectic crystal.	3	30/09/2019-03/10/2019	J.-M. Zanotti
CRG-2669	**PLAZANET Marie**: LIPHY UG SAINT MARTIN D HERES	Transport of water in soft confinement: influence of surface chemistry	4	03/10/2019-07/10/2019	Q. Berrod J.-M. Zanotti
6-01-332	**GORELLI Federico Aiace**: CNR - INO, FIRENZE	Collective dynamics of fluid Neon in the supercritical regime	4	07/10/2019-11/10/2019	M. Koza
7-01-508	**NEMES Norbert**: FAC CIEN FIS, UNIV COMPLUTENSE	Phonon softening and lattice thermal conductivity in SnSe thermoelectrics: temperature and dopant dependence	3	11/10/2019-14/10/2019	M. Koza
7-03-182	**MURSHED Mohammad Mangir**: INST INORG & PHYS CHEM, BREMEN	Lithium diffusion in Li0.4WO3 bronze studied by quasi-elastic neutronscattering	1	14/10/2019-15/10/2019	M. Koza

Cycle 187

Proposal	Main Proposer	Title	# of Days	Schedule dates	Local Contact
CRG-2684	**CORMIER Laurent**: IMPMC, PARIS	Dynamic properties of Li-borate glasses with a reversibility window	5	09/01/2020-14/01/2020	ZANOTTI Jean-Marc
6-02-600	**FORMISANO Ferdinando**: CNR-IOM/OGG	Dynamics in water-nanoparticles colloidal suspensions.	2	14/01/2020-16/01/2020	ZANOTTI Jean-Marc

1-04-172	**NOGUERE Gilles**: CEA SAINT PAUL LEZ DURANCE	Measurements of the double-differential neutron cross-section of U inUO2 up-1600 K	4	16/01/2020-20/01/2020	ZANOTTI Jean-Marc
7-05-509	**TRAEGER Franziska**: WESTFÄLISCHE HOCHSCHULE ,GELSENKIRCHEN	Diffusion of water and hydrogen inMoS2 (single crystal and powder)	3	20/01/2020-23/01/2020	KOZA Michael Marek
4-05-752	**KERMARREC Edwin**: CNRS/LABORATOIRE DE PHYS D SOLIDES (LPS)	Quantum spin liquid in Seff=1/2 frustrated antiferromagnets with strong spin-orbit coupling	5	23/01/2020-28/01/2020	ZANOTTI Jean-Marc
7-03-178	**FAMPRIKIS Theodosios**: LRCS-UPJV, AMIENS	Elucidation of ion dynamics in Li3PS4 solid electrolytes for all solid-state batteries by means of inelastic neutron scattering	3	28/01/2020-31/01/2020	ZBIRI Mohamed
CRG-2701	**ZANOTTI Jean-Marc**: CNCE/LLB, CEA SACLAY	2D dynamics of electrolytes under confinement in pillared graphene-based materials	5	31/01/2020-05/02/2020	ZANOTTI Jean-Marc, BERROD Quentin
CRG-2683	**LYONNARD Sandrine**: UMR SYMMMES	Ion dynamics in Thermotropic IonicLiquid Crystals	5	05/02/2020-10/02/2020	ZANOTTI Jean-Marc, BERROD Quentin
7-01-501	**D'AMBRUMENIL Stella**: ILL, GRENOBLE	Metallophilic interaction in the phonon dynamics of the colossal thermal expansion framework materials: M3[Co(CN)6] (M = H, Cu, Ag)	2	10/02/2020-12/02/2020	ZBIRI Mohamed
7-01-502	**D'AMBRUMENIL Stella**: ILL, GRENOBLE	Phonon behavior under pressure of1D negative thermal expansion group 11 cyanides	3	12/02/2020-15/02/2020	ZBIRI Mohamed
CRG-2670	**CANDOLFI Christophe**: INST LAMOUR VANDOEUVRE NANCY	Probing the anharmonicity of the lattice dynamics of the cluster compound Ag3RbMo9Se11 by inelastic neutron scattering	3	15/02/2020-18/02/2020	ZANOTTI Jean-Marc
EASY-537	**PLAZANET Marie**: LIPHY UG SAINT MARTIN D HERES	Water diffusion into ZIF-8 hydrophobic nanopores	3	18/02/2020-21/02/2020	ZANOTTI Jean-Marc
4-06-10	**GOBAUT Benoit**: LABORATOIRE LÉON BRILLOUIN UMR12 CEA-CNRS	Studying the ZFS terms in photoswitchable Prussian Blue Analog nanoparticles.	4	21/02/2020-25/02/2020	BERROD Quentin

Cycle 188					
CRG-2745	**PIN Serge**: CEA SACLAY ,GIF-SUR-YVETTE	Study of the dynamic of hemoglobin hydrogel	1	11/08/2020-12/08/2020	ZANOTTI Jean-Marc
CRG-2730	**JACQUEMIN Maxime**: CNRS/CEMHTI, ORLEANS	Quasi elastic neutron scattering on dosium calcium aluminosilicate (NCAS) melts	2	12/08/2020-14/08/2020	ZANOTTI Jean-Marc
CRG-2728	**MISURACA Loreto**: ILL, GRENOBLE	Understanding the high-temperature molecular motion of a model protomembrane architecture	3	14/08/2020-17/08/2020	ZANOTTI Jean-Marc
CRG-2742	**ALBA SIMIONESCO Christiane**: CEA - DSM/IRAMIS/LLB/ GSBD ,GIF-SUR-YVETTE	Dynamical processes of supra-molecular liquids, case of mono-alcoholsC8H17OH	2	17/08/2020-19/08/2020	ZANOTTI Jean-Marc, BERROD Quentin
7-03-187	**EVANS Ivana**: DEPT CHEM, UNIV DURHAM	Fluorite-type solid electrolytes with complex oxide ion diffusion mechanisms	3	19/08/2020-22/08/2020	BERROD Quentin
7-03-189	**EVANS Ivana**: DEPT CHEM, UNIV DURHAM	Oxide ions diffusion mechanism in melilite-type solid electrolytes	2	22/08/2020-24/08/2020	BERROD Quentin
CRG-2725	**SIMONET Virginie**: CNRS GRENOBLE - INSTITUT NEEL	Crystal field level transitions in frustrated Tb2NbScO7 pyrochlore prone-charge disorder	3	24/08/2020-27/08/2020	PETIT Sylvain
CRG-2729	**PETIT Sylvain**: CNCE/LLB, CEA SACLAY	Spin dynamics in Nd3Ga5O12	4	28/08/2020-01/09/2020	PETIT Sylvain
CRG-2745	**PIN Serge**: CEA SACLAY ,GIF-SUR-YVETTE	Study of the dynamic of hemoglobin hydrogel	1	27/08/2020-28/08/2020	ZANOTTI Jean-Marc
CRG-2764	**PLAZANET Marie**: LIPHY UG SAINT MARTIN D HERES	Transport of water in soft confinement	3	01/09/2020-04/09/2020	ZANOTTI Jean-Marc
4-02-579	**KHIM Seunghyun**: MAX-PLANCK INSTITUTE CPFS ,DRESDEN	Magnetic excitations in the new heavy-fermion superconductor CeRh2As2	4	04/09/2020-08/09/2020	KOZA Michael Marek
CRG-2727	**KERMARREC Edwin**: CNRS/LABORATOIRE DE PHYS D SOLIDES (LPS), ORSAY	Probing low lying spin excitations in triangular magnet ErMgGaO4	3	08/09/2020-11/09/2020	PETIT Sylvain
7-01-511	**NISHIYAMA Yoshiharu**: CNRS-CERMAV	Acoustic phonon dispersion along the chain of fully deuterated cellulose crystal	3	11/09/2020-14/09/2020	ZANOTTI Jean-Marc

4-06-11	**MUTSCHLER Julius**: FAK PHYS, UNIV FREIBURG	Study of a Novel Series of Isostructural Heterometallic 3d-4f Single Molecule Magnets with INS	3	14/09/2020-17/09/2020	ZANOTTI Jean-Marc
CRG-2721	**JUDEINSTEIN Patrick**: CNCE/LLB, CEA SACLAY	Elementary mechanisms in gas separation using zeolite membranes: experiment and molecular modeling	4	17/09/2020-21/09/2020	BERROD Quentin, ZANOTTI Jean-Marc
1-04-184	**NOGUERE Gilles**: CEA SAINT PAUL LEZ DURANCE	Measurements of the double-differential neutron cross section of ThO2 , U3O8 and UAl at room temperature	2	21/09/2020-23/09/2020	BERROD Quentin, ZANOTTI Jean-Marc
CRG-2743	**GIORDANO Valentina**: ILM - UCBL 1, VILLEURBANNE	Evidencing the interface effect on the phonon dynamics in a TiO2 nanopowder material	3	23/09/2020-26/09/2020	ZANOTTI Jean-Marc

Cycle 189
SHARP
Construction: No experiments

Cycle 190
Commissioning
No experiments

Cycle 191
SHARP is welcoming its first users

Proposal #	First applicant	Title	# of days	Schedule dates	Local Contact
9-11-1980	**FOGLIA Fabrizia** UNIVERSITY COLLEGE LONDON	Dynamical characterization of a new sandwiched multicomponent membrane for energy applications	3	03/09/2021-06/09/2021	Berrod Zanotti
7-05-515	**ASLAN Neslihan**, HELMHOLTZ-ZENTRUM MAX-PLANCK-STR. 1 21502 GEESTHACHT	In-situ QENS investigation of Compl ex Hydrides	3	06/09/2021-09/09/2021	Berrod Zanotti
6-07-77	**CLANCY Adam**, UNIVERSITY COLLEGE LONDON	Electrolyte Dynamics in PhosphorusNanoribbon Based	4	09/09/2021-13/09/2021	Berrod Zanotti

		Metal-Ion Batteries			
CRG-1358	**Edwin Kermarrec**, CNRS/LABORATOIRE DE PHYS D BATIMENT 510, UMR 8502 UNIVERSITE PARIS SUD XI 91405 ORSAY	Quantum excitations and 2D spin liquid correlations in triangular antiferromagnets	3	13/09/2021-16/09/2021	Petit Berrod
CRG-2896	**Denis Morineau**, IPR - UNIV RENNES 1 INST DE PHYS DE RENNES - UMR CNRS 6251 263 AV. GÉNÉRAL LECLERC 35042 RENNES	Water dynamics in mesopores with a periodic distribution of ionic surface charge.	4	16/09/2021-20/09/2021	Zanotti
7-02-205	**SENN Mark**, DEPT CHEMISTRY UNIVE GIBBET HILL ROAD cv4 7al COVENTRY UNITED KINGDOM	Characterising the soft modes in NTE material Ca2Mn1-yTiyO4	3	20/09/2021/23/09/2021	Berrod Zanotti
CRG-2897	**Christophe Candolfi**, INST LAMOUR VANDOEUVRE 54506 VANDOEUVRE LES NANC	Influence of crystal symmetry on the lattice dynamics of the thermoelectric Cu2+xSn1-xS3 phase	2	23/09/2021-25/09/2021	Zanotti
CRG-2894	**Sylvain Petit**, Laboratoire Léon Brillouin, CEA Saclay, Gif-sur-Yvette cedex	Spin dynamics in (NdLa)2Zr2O7 pyrochlore magnets	4	21/09/2021-01/10/2021	Petit Berrod
CRG-2906	**Arianna D'ANGELO**, CNRS/LABORATOIRE DE PHYS D BATIMENT 510, UMR 8502 UNIVERSITE PARIS SUD XI 91405 ORSA	Understanding the Diffusion of Water inside Ge-based Imogolite NanoTubes	3	01/10/2021-04/10/2021	Zanotti
CRG-1363	**Patrick Judeinstein**, Laboratoire Léon Brillouin, CEA Saclay, Gif-sur-Yvette cedex	Elementary Mechanisms in Gas Separation using Zeolite Membranes:	4	04/10/2021-08/10/2021	Berrod Zanotti

		Experiment and Molecular Modeling			
6-07-73	**Q. Berrod**, IRIG/SyMMES, CNRS/UMR 5819, 17 RUE DES MARTYRS, F-38054 GRENOBLE	Dynamics of a Polymer Electrolytein bulk and under 1D CNT nanometricconfinement	3	08/12/2021-12/10/2021	Berrod Zanotti
TEST-3251	**FANs du LLB**	IL in CNT / Mn12 Acetate	1	12/10/2021-13/10/2021	Berrod Petit

XII. List of publications

YEAR 2018

1- Journals articles :

1. Anand, V. K. et al. Understanding the magnetism in noncentrosymmetric CeIrGe 3 : Muon spin relaxation and neutron scattering studies. Phys. Rev. B 97, 184422 (2018).

2. Andersson, C. D. et al. Influence of Enantiomeric Inhibitors on the Dynamics of Acetylcholinesterase Measured by Elastic Incoherent Neutron Scattering. J. Phys. Chem. B 122, 8516–8525 (2018).

3. Bloodworth, S. et al. Synthesis and Properties of Open Fullerenes Encapsulating Ammonia and Methane. ChemPhysChem 19, 266–276 (2018).

4. Browne, A. J., Lithgow, C., Kimber, S. A. J. & Attfield, J. P. Orbital Molecules in the New Spinel GaV2O4. Inorg. Chem. 57, 2815–2822 (2018).

5. d'Ambrumenil, S. et al. Lattice dynamics and negative thermal expansion in the framework compound ZnNi (CN) 4 with two-dimensional and three-dimensional local environments. Phys. Rev. B 99, 024309 (2019).

6. Dian, E. et al. Scattered neutron background in thermal neutron detectors. Nuclear Instruments and Methods in Physics Research Section A: Accelerators, Spectrometers, Detectors and Associated Equipment 902, 173–183 (2018).

7. Fuller, C. A. et al. Brownmillerite-Type Sr 2 ScGaO 5 Oxide Ion Conductor: Local Structure, Phase Transition, and Dynamics. Chem. Mater. acs.chemmater.9b02051 (2019).

8. Hansen, H. W., Sanz, A., Adrjanowicz, K., Frick, B. & Niss, K. Evidence of a one-dimensional thermodynamic phase diagram for simple glass-formers. Nat Commun 9, 518 (2018).

9. Lorne, T. et al. Investigation of the grafting of fluorophores onto double-walled carbon nanotubes: The influence of the geometry of the molecules. Applied Surface Science 457, 1181–1191 (2018).

10. Mishra, S. K. et al. Presence of water at elevated temperatures, structural transition, and thermal expansion behavior in LaP O 4: Eu. Phys. Rev. Materials 2, 126003 (2018).

11. Mittal, R., Gupta, M. K. & Chaplot, S. L. Phonons and anomalous thermal expansion behaviour in crystalline solids. Progress in Materials Science 92, 360–445 (2018).

12. Nair, H. S. et al. Absence of a long-range ordered magnetic ground state in Pr 3 Rh 4 Sn 13 studied through specific heat and inelastic neutron scattering. J. Phys.: Condens. Matter 30, 145601 (2018).

13. Pajzderska, A. et al. Diversity of methyl group dynamics in felodipine: a DFT supported NMR and QENS study. CrystEngComm 20, 7371–7385 (2018).

14. Peet, J. R., Chambers, M. S., Piovano, A., Johnson, M. R. & Evans, I. R. Dynamics in Bi(III)-containing apatite-type oxide ion conductors: a combined computational and experimental study. J. Mater. Chem. A 6, 5129–5135 (2018).

15. Peters, J. et al. New pressure cells for membrane layers and systems in solutions up to 100°C. Journal of Neutron Research 20, 3–12 (2018).

16. Sanz, A. et al. High-pressure cell for simultaneous dielectric and neutron spectroscopy. Review of Scientific Instruments 89, 023904 (2018).

17. Sassi, S., Candolfi, C., Dauscher, A., Lenoir, B. & Koza, M. M. Inelastic neutron scattering study of the lattice dynamics of the homologous compounds (PbSe) 5 (Bi 2 Se 3) 3m (m = 1, 2 and 3). Phys. Chem. Chem. Phys. 20, 14597–14607 (2018).

18. Singh, B. et al. Anomalous Lattice Dynamics in AgC4N3: Insights From Inelastic Neutron Scattering and Density Functional Calculations. Front. Chem. 6, 544 (2018).

19. Sprick, R. S. et al. Photocatalytic Hydrogen Evolution from Water Using Fluorene and Dibenzothiophene Sulfone-Conjugated Microporous and Linear Polymers. Chem. Mater. 31, 305–313 (2019).

20. Tamtögl, A. et al. Ultrafast molecular transport on carbon surfaces: The diffusion of ammonia on graphite. Carbon 126, 23–30 (2018).

2- Book:

21. Stadler, A. M. Conformational Motions of Disordered Proteins. in Biological, Physical and Technical Basics of Cell Engineering (eds. Artmann, G. M., Artmann, A., Zhubanova, A. A. & Digel, I.) 381–399 (Springer Singapore, 2018).

3- *PhD* thesis:

22. Hansen, H. W. Dynamics of glass-forming liquids: Will theory and experiment ever meet? (Roskilde University, 2018).

23. Peet, J. R. Oxide ion conductors for energy applications: structure, dynamics and properties. (Durham University, 2018).

24. Piazza, I. Water Dynamics in Biological Systems investigated using Neutron Scattering Techniques. (Università degli Studi di Palermo, 2018).

25. Ranieri, U. Guest dynamics in methane hydrates and hydrogen hydrates under high pressure. (École Polytechnique Fédérale de Lausanne, 2018).

YEAR 2019

1. Laulumaa, S., Koza, M. M., Seydel, T., Kursula, P. & Natali, F. A Quasielastic Neutron Scattering Investigation on the Molecular Self-Dynamics of Human Myelin Protein P2. *J. Phys. Chem. B* **123**, 8178–8185 (2019).

2. d'Ambrumenil, S. *et al.* Anomalous thermal expansion in one-dimensional transition metal cyanides: Behavior of the trimetallic cyanide C u 1 / 3 A g 1 / 3 A u 1 / 3 CN. *Phys. Rev. B* **100**, 174302 (2019).

3. Saouessi, M., Peters, J. & Kneller, G. R. Asymptotic analysis of quasielastic neutron scattering data from human acetylcholinesterase reveals subtle dynamical changes upon ligand binding. *J. Chem. Phys.* **150**, 161104 (2019).

4. Fuller, C. A. *et al.* Brownmillerite-Type Sr $_2$ ScGaO $_5$ Oxide Ion Conductor: Local Structure, Phase Transition, and Dynamics. *Chem. Mater.* acs.chemmater.9b02051 (2019) doi:10.1021/acs.chemmater.9b02051.

5. Golub, M. *et al.* Dynamics of a family of cyan fluorescent proteins probed by incoherent neutron scattering. *J. R. Soc. Interface* **16**, 20180848 (2019).

6. Russo, D., Lambreva, M. D., Simionesco, C. A., Sebban, P. & Rea, G. Dynamics Properties of Photosynthetic Microorganisms Probed by Incoherent Neutron Scattering. *Biophys. J.* **116**, 1759–1768 (2019).

7. Saouessi, M., Peters, J. & Kneller, G. R. Frequency domain modeling of quasielastic neutron scattering from hydrated protein powders: Application to free and inhibited human acetylcholinesterase. *J. Chem. Phys.* **151**, 125103 (2019).

8. Foglia, F. *et al.* In Vivo Water Dynamics in Shewanella oneidensis Bacteria at High Pressure. *Sci. Rep.* **9**, 8716 (2019).

9. Peet, J. R. *et al.* Insight into Design of Improved Oxide Ion Conductors: Dynamics and Conduction Mechanisms in the Bi $_{0.913}$ V $_{0.087}$ O $_{1.587}$ Solid Electrolyte. *J. Am. Chem. Soc.* **141**, 9989–9997 (2019).

10. d'Ambrumenil, S. *et al.* Lattice dynamics and negative thermal expansion in the framework compound ZnNi (CN) 4 with two-dimensional and three-dimensional local environments. *Phys. Rev. B* **99**, 024309 (2019).

11. Guilbert, A. A. Y. *et al.* Mapping Microstructural Dynamics up to the Nanosecond of the Conjugated Polymer P3HT in the Solid State. *Chem. Mater.* **31**, 9635–9651 (2019).

12. d'Ambrumenil, S., Zbiri, M., Chippindale, A. M. & Hibble, S. J. Phonon dynamics in the layered negative thermal expansion compounds C u x N i 2 − x (CN) 4. *Phys. Rev. B* **100**, 094312 (2019).

13. Sprick, R. S. *et al.* Photocatalytic Hydrogen Evolution from Water Using Fluorene and Dibenzothiophene Sulfone-Conjugated Microporous and Linear Polymers. *Chem. Mater.* **31**, 305–313 (2019).

14. Ranieri, U. *et al.* Quantum Dynamics of H $_2$ and D $_2$ Confined in Hydrate Structures as a Function of Pressure and Temperature. *J. Phys. Chem. C* **123**, 1888–1903 (2019).

15. Weis, H. *et al.* Self- and interdiffusion in dilute liquid germanium-based alloys. *J. Phys. Condens. Matter* **31**, 455101 (2019).

16. Lefrançois, E. *et al.* Spin decoupling under a staggered field in the Gd 2 Ir 2 O 7 pyrochlore. *Phys. Rev. B* **99**, 060401 (2019).

17. Doster, W. Time domain versus energy domain neutron scattering analysis of protein dynamics. *Proc. Natl. Acad. Sci.* **116**, 8649–8650 (2019).

18. Łuczyńska, K., Drużbicki, K., Runka, T., Pałka, N. & Węsicki, J. Vibrational Response of Felodipine in the THz Domain: Optical and Neutron Spectroscopy Versus Plane-Wave DFT Modeling. *J. Infrared Millim. Terahertz Waves* (2019) doi:10.1007/s10762-019-00634-9.

YEAR 2020

1. Bahn E., Hoyos Giraldo L.A., Kuznetsov V., Calvo-Almazán I., Zbiri M., Koza M.M., Hansen T.C., Henry P.F., Lapp A., Pouget S., Mesa M., Fouquet P. - Ultra-fast diffusion of hydrogen in a novel mesoporous N-doped carbon
Carbon 166, 307-315 (2020)
Domain: Spectroscopy in Solid State Physics and Chemistry

2. Candolfi C., Guélou G., Bourgès C., Supka A.R., Al Rahal Al Orabi R., Fornari M., Malaman B., Le Caër G., Lemoine P., Hardy V., Zanotti J.M., Chetty R., Ohta M., Suekuni K., Guilmeau E. - Disorder-driven glasslike thermal conductivity in colusite Cu26V2Sn6S32 investigated by Mössbauer spectroscopy and inelastic neutron scattering
Physical Review Materials 4, 025404-1-025404-10 (2020)
Domain: Spectroscopy in Solid State Physics and Chemistry

3. Candolfi C., Koza M.M., Aydemir U., Carrillo-Cabrera W., Grin Y., Steglich F., Baitinger M. - Vibrational dynamics of the type-I clathrates A8Sn44□2 (A = Cs, Rb, K) from lattice-dynamics calculations, inelastic neutron scattering, and specific heat measurements
Journal of Applied Physics 127, 145104-1-145104-15 (2020)
Domain: Spectroscopy in Solid State Physics and Chemistry

4. Cathelin V., Lefrançois E., Robert J., Guruciaga P.C., Paulsen C., Prabhakaran D., Lejay P., Damay F., Ollivier J., Fåk B., Chapon L.C., Ballou R., Simonet V., Holdsworth P.C.W., Lhotel E. - Fragmented monopole crystal, dimer entropy, and Coulomb interactions in Dy2Ir2O7
Physical Review Research 2, 032073-1-032073-6 (2020)
Domain: Magnetic Excitations

5. Famprikis T., Kudu Ö.U., Dawson J.A., Canepa P., Fauth F., Suard E., Zbiri M., Dambournet D., Borkiewicz O.J., Bouyanfif H., Emge S.P., Cretu S., Chotard J.N., Grey C.P., Zeier W.G., Islam M.S., Masquelier C. - Under pressure: Mechanochemical effects on structure and ion conduction in the sodium-ion solid electrolyte Na3PS4
Journal of the American Chemical Society 142, 18422-18436 (2020)
Domain: Crystallography and Chemistry

6. Fuller C.A., Berrod Q., Frick B., Johnson M.R., Avdeev M., Evans J.S.O., Evans I.R. - Oxide ion and proton conductivity in highly oxygen-deficient cubic perovskite SrSc0.3Zn0.2Ga0.5O2.4
Chemistry of Materials 32, 4347-4357 (2020)
Domain: Spectroscopy in Solid State Physics and Chemistry

7. Gainza J., Serrano-Sánchez F., Rodrigues J.E.F.S., Huttel Y., Durá O.J., Koza M.M., Fernández-Díaz M.T., Meléndez J.J., Markus B.G., Simon F., Martínez J.L., Alonso J.A., Nemes N.M. - High-performance n-type SnSe thermoelectric polycrystal prepared by arc-melting
Cell Reports Physical Science 1, 100263-1-100263-20 (2020)
Domain: Spectroscopy in Solid State Physics and Chemistry

8. Hayashida S., Ishikawa H., Okamoto Y., Okubo T., Hiroi Z., Nilsen G.J., Mutka H., Masuda T. - Zero-energy excitation in the classical kagome antiferromagnet NaBa2Mn3F11
Physical Review B 101, 214409-1-214409-6 (2020)
Domain: Magnetic Excitations

9. Lushchekina S.V., Inidjel G., Martinez N., Masson P., Trovaslet-Leroy M., Nachon F., Koza M.M., Seydel T., Peters J. - Impact of sucrose as osmolyte on molecular dynamics of mouse acetylcholinesterase
Biomolecules 10, 1664-1-1664-19 (2020)
Domain: Biology

10. Nikitin S.E., Franco D.G., Kwon J., Bewley R., Podlesnyak A., Hoser A., Koza M.M., Geibel C., Stockert O. - Gradual pressure-induced enhancement of magnon excitations in CeCoSi
Physical Review B 101, 214426-1-214426-11 (2020)
Domain: Magnetic Excitations

11. Noguere G., Scotta J.P., Xu S., Filhol A., Ollivier J., Farhi E., Calzavarra Y., Rols S., Fåk B., Zanotti J.M., Berrod Q. - Combining density functional theory and Monte Carlo neutron transport calculations to study the phonon density of states of UO2 up to 1675 K by inelastic neutron scattering
Physical Review B 102, 134312-1-134312-12 (2020)
Domain: Spectroscopy in Solid State Physics and Chemistry

12. Schirò G. - Probing the dynamics of biological matter by elastic, quasi-elastic, and inelastic neutron scattering
EPJ Web of Conferences 236, 05001-1-05001-18 (2020)
Domain: Biology

13. Singh B., Gupta M.K., Mittal R., Zbiri M., Ravindran T.R., Schober H., Chaplot S.L. - Phonons and anomalous lattice behavior in KMnAg3(CN)6 and KNiAu3(CN)6: Inelastic neutron scattering and first-principles calculations
Journal of Physical Chemistry C 124, 7216-7228 (2020)
Domain: Theory

14. Songvilay M., Petit S., Koza M., Rols S., Suard E., Skumryev V., Martin C., Damay F. - Disorder and magnetic excitations in CaCrxFe2-xO4 (x=0,0.5)
Physical Review B 101, 014407-1-014407-9 (2020)
Domain: Magnetic Excitations

15. Stockert O., Hoffmann J.U., Mühlbauer M., Senyshyn A., Koza M.M., Tsirlin A.A., Wolf F.M., Bachus S., Gegenwart P., Movshovich R., Bobev S., Fritsch V. - Magnetic frustration in a metallic fcc lattice
Physical Review Research 2, 013183-1-013183-12 (2020)
Domain: Magnetic Excitations

16. Viennois R., Hermet P., Machon D., Koza M.M., Bourgogne D., Fraisse B., Petrović A.P., Maurin D. - Stability and lattice dynamics of Ruddlesden-Popper tetragonal Sr2TiO4
Journal of Physical Chemistry C 124, 27882-27893 (2020)
Domain: Spectroscopy in Solid State Physics and Chemistry

17. Łuczyńska K., Drużbicki K., Runka T., Pałka N., Wasicki J. - Vibrational response of felodipine in the THz domain: Optical and neutron spectroscopy versus plane-wave DFT modeling
International Journal of Infrared and Millimeter Waves 41, 1301-1336 (2020)
Domain: Theory

YEAR 2021

1. Famprikis, T., H. Bouyanfif, P. Canepa, M. Zbiri, J.A. Dawson, E. Suard, F. Fauth, H.Y. Playford, D. Dambournet, O.J. Borkiewicz, M. Courty, O. Clemens, J.-N. Chotard, M.S. Islam, and C. Masquelier. 2021. Insights into the Rich Polymorphism of the Na+ Ion Conductor Na3PS4 from the Perspective of Variable-Temperature Diffraction and Spectroscopy. Chem. Mater. 33:5652–5667.

2. Guilbert, A.A.Y., Y. Bai, C.M. Aitchison, R.S. Sprick, and M. Zbiri. 2021. Impact of Chemical Structure on the Dynamics of Mass Transfer of Water in Conjugated Microporous Polymers: A Neutron Spectroscopy Study. ACS Appl. Polym. Mater. 3:765–776.

3. Guilbert, A.A.Y., Z.S. Parr, T. Kreouzis, D.J. Woods, R.S. Sprick, I. Abrahams, C.B. Nielsen, and M. Zbiri. 2021. Effect of substituting non-polar chains with polar chains on the structural dynamics of small organic molecule and polymer semiconductors. Phys. Chem. Chem. Phys. 23:7462–7471.

4. Zbiri, M., P.A. Finn, C.B. Nielsen, and A.A.Y. Guilbert. 2021. Quantitative insights into the phase behaviour and miscibility of organic photovoltaic active layers from the perspective of neutron spectroscopy. J. Mater. Chem. C. 9:11873–11881.

5. Köhler, T., M. Zschornak, M. Zbiri, J. Hanzig, C. Röder, C. Funke, H. Stöcker, E. Mehner, and D.C. Meyer. 2021. Defect formation in chemically reduced congruent LiTaO 3 : ab initio simulations and inelastic neutron scattering. J. Mater. Chem. C. 9:13484–13499.

6. Laurell, P., A. Scheie, C.J. Mukherjee, M.M. Koza, M. Enderle, Z. Tylczynski, S. Okamoto, R. Coldea, D.A. Tennant, and G. Alvarez. 2021. Quantifying and Controlling Entanglement in the Quantum Magnet Cs 2 CoCl 4. Phys. Rev. Lett. 127:037201.

7. Le Caër, S., M.-C. Pignié, Q. Berrod, V. Grzimek, M. Russina, C. Carteret, A. Thill, J.-M. Zanotti, and J. Teixeira. 2021. Dynamics in hydrated inorganic nanotubes studied by neutron scattering: towards nanoreactors in water. Nanoscale Adv. 3:789–799.

8. Misuraca, L., B. Deme, J. Peters, and P. Oger. 2019. Protomembranes at the origin of life. Eur. Biophys. J. Biophys. Lett. 48:S109–S109.

9. Petit, S., F. Damay, Q. Berrod, and J.M. Zanotti. 2021. Spin and lattice dynamics in the two-singlet system Tb 3 Ga 5 O 12. Phys. Rev. Research. 3:013030.

10. Ranieri, U., S. Klotz, R. Gaal, M.M. Koza, and L.E. Bove. 2021. Diffusion in dense supercritical methane from quasi-elastic neutron scattering measurements. Nat Commun. 12:1958.

11. Stoeckel, M.-A., Y. Olivier, M. Gobbi, D. Dudenko, V. Lemaur, M. Zbiri, A.A.Y. Guilbert, G. D'Avino, F. Liscio, A. Migliori, L. Ortolani, N. Demitri, X. Jin, Y.-G. Jeong, A. Liscio, M.-V. Nardi, L. Pasquali, L. Razzari, D. Beljonne, P. Samorì, and E. Orgiu. 2021. Analysis of External and Internal Disorder to Understand Band-Like Transport in n-Type Organic Semiconductors. Advanced Materials. 33:2007870.

12. Vaunat, A., V. Balédent, S. Petit, P. Roy, J.B. Brubach, G. Giri, E. Rebolini, P. Steffens, S. Raymond, Q. Berrod, M.B. Lepetit, and P. Foury-Leylekian. 2021. Evidence for an electromagnon in GdMn 2 O 5 : A multiferroic with a large electric polarization. Phys. Rev. B. 103:174434.

13. Wolanin, J., J. Giraud, C. Payre, M. Benoit, C. Antonelli, D. Quemener, I. Tahiri, M. Vandamme, J.-M. Zanotti, and M. Plazanet. 2021. Oedometric-like setup for the study of water transport in porous media by quasi-elastic neutron scattering. Review of Scientific Instruments. 92:024106.

14. Wolanin, J., L. Michel, D. Tabacchioni, J.M. Zanotti, J. Peters, I. Imaz, B. Coasne, M. Plazanet, and C. Picard. 2021. Heterogeneous Microscopic Dynamics of Intruded Water in a Superhydrophobic Nanoconfinement: Neutron Scattering and Molecular Modeling. J. Phys. Chem. B. 125:10392–10399.

15. Noguere, G., J.P. Scotta, S. Xu, E. Farhi, J. Ollivier, Y. Calzavarra, S. Rols, M. Koza, and J.I. Marquez Damian. 2021. Temperature-dependent dynamic structure factors for liquid water inferred from inelastic neutron scattering measurements. J. Chem. Phys. 155:024502.

PhDs:

16- **Rasmus LAVEN**

Neutron spectroscopy studies of vibrational and diffusional dynamics in organometal halide and oxyhydride perovskites

Department of Chemistry and Chemical Engineering

CHALMERS UNIVERSITY OF TECHNOLOGY

Göteborg, Sweden 2021

17- **Loreto MISURACA**
Les protomembranes à l'origine de la vie, Protomembranes at the origin of life
Grenoble, France, March 22 2021

18- **Shelby TURNER**
The investigation of phonon lifetime and thermal transport mechanisms in complex and disordered crystalline systems by means of inelastic neutron and X-ray spectroscopy
October 22nd 2021
Grenoble, France

YEAR 2022
(January to June)

1. Bicout, D.J., A. Cisse, T. Matsuo, and J. Peters. 2022. The dynamical Matryoshka model: 1. Incoherent neutron scattering functions for lipid dynamics in bilayers. Biochimica et Biophysica Acta (BBA) - Biomembranes. 1864:183944.

2. Matsuo, T., A. Cisse, M. Plazanet, F. Natali, M.M. Koza, J. Ollivier, D.J. Bicout, and J. Peters. 2022. The dynamical Matryoshka model: 3. Diffusive nature of the atomic motions contained in a new dynamical model for deciphering local lipid dynamics. Biochimica et Biophysica Acta (BBA) - Biomembranes. 1864:183949.

3. Viennois, R., M. Beaudhuin, and M.M. Koza. 2022. Strong renormalization of Ba vibrations in thermoelectric type-IX clathrate Ba 24 Ge 100. Phys. Rev. B. 105:054314.

4. Misuraca, L., T. Matsuo, A. Cisse, J. LoRicco, A. Caliò, J.-M. Zanotti, B. Demé, P. Oger, and J. Peters. 2022. High temperature molecular motions within a model protomembrane architecture. Phys. Chem. Chem. Phys. 24:15083–15090.

5. Foglia, F., Q. Berrod, A.J. Clancy, K. Smith, G. Gebel, V.G. Sakai, M. Appel, J.-M. Zanotti, M. Tyagi, N. Mahmoudi, T.S. Miller, J.R. Varcoe, A.P. Periasamy, D.J.L. Brett, P.R. Shearing, S. Lyonnard, and P.F. McMillan. 2022. Disentangling water, ion and polymer dynamics in an anion exchange membrane. Nat. Mater. 21:555–563.

PhD:
6- **Vitalii KUZNETSOV**
HYDROGEN DYNAMICS IN ELEMENTARY REACTIONS ON MOLYBDENUM COMPOUNDS
April 6, 2022.
Grenoble, France

XIII. Scientific highlight – Full text

See Annex 3.

ANNEX 1

Beam-time use on IN6-SHARP over the period 2018 to 2020.

IN6-SHARP									
Year	2018			2019		2020		Total	Average
Cycle #	182	183	184	185	186	187	188		
Start date	01/03/2018	22/05/2018	03/09/2018	13/06/2019	28/08/2019	09/01/2020	11/08/2020		
End date	25/04/2018	12/07/2018	28/10/2018	04/08/2019	15/10/2019	26/02/2020	28/09/2020		
Expected Cycle Duration	49	51	55	52	48	48	48	351	
Expected Total Cycle Duration: $S_{Reactor}$	155			100		96			
Reactor Shutdown	2	6	3	2	0	2	0	15	
Total Reactor Shutdown	11			2		2			
Commissioning	9			1		3		13	
Comment Commissioning	4.5 days for CRG and 4.5 days for ILL commissioning after 2017 long shutdown			1 day at reactor restart		1.5 day CRG and 1.5 day ILL reactor restart			
Instrument Failure	3			2		0		5	
Reason For failure	Chopper Electronic Failure			Secondary Shutter failure		Secondary Shutter failure			
Other days lost	2			3		1		6	
Reason day lost	Health Physics tests for bi-decenal instrument clearance after "Instrument Safety File"			Waiting for Health Physics Clearance		Samp. Env. failure (sample licking in furnace)			
Days lost S_L (commissioning included)	25			8		6		39	
Total Research Effective Beamtime: $S_{REBT} = S_{Reactor} - S_{lost}$	130			92		90		312	
Fraction of Research Effective Beam-time: $S_{REBT} / S_{Reactor}$	**84%**			**92%**		**94%**			**89%**
S_{CRG}: CRG Research Effective Beam time	68			54		45		167	
CRG : Fraction of Research Beam-time: S_{CRG}/S_{REBT}	**52%**			**59%**		**50%**			**54%**
S_{ILL}: ILL Research Effective Beam time	60			38		45		143	
ILL : Fraction of Research Beam-time: S_{ILL}/S_{REBT}	**46%**			**41%**		**50%**			**46%**
S_T: Training	2							2	
Training type	HERCULES practical: Soft Matter & Solid State Physics								
Training : Fraction of Effective beam time: S_T/S_{REBT}	2%			0%		0%			1%

Table 1. Beam-time use on IN6-SHARP over the period 2018 to 2020 (numbers are expressed in “days”).

ANNEX 2

ILL and LLB people involved in the SHARP project
next to the scientific and technical teams

But also:

- **Bureau d'étude :** L. Didier, P. Permingeat, B. Giroud
- **Hall :** B. Jarry
- **Aménagement :** P. Coggo
- **Mécanique / Usinage :** J. Beaucourt, F. Lapeyre, O. Tessier
- **Détecteurs :** J.-C. Buffet, B. Guérard, J. Marchal, F. Pinet, J. Pentenero, S. Cuccaro
- **SCI :** J.-M. Delpierre, J. Blanc-Pacques, S. Sallaz-Damaz
- **Vide :** E. Iampasona, A. Girault
- **Automatismes :** C. Mounier, B. Sornin
- **Electronique & DAS :** P. Mutti, Y. Le Goc
- **Monochromateur :** P. Courtois
- **Sécurité :** I. Perbet, G. Bonnet
- **Radio-Protection :** F. Rencurel, S. Grimaud, P. Cochet
- **Administratifs :** A. Verdier, S. Même, O. Sineau, E. Colas, P. Combrisson
- **Service Commercial CEA :** A. Rozier, C. Berthon
- **Planning :** M. Plassard
- **Groupes Spectroscopie :** B. Farago, S. Petit
- **CEA/DRF & IRAMIS :** H. Desvaux, F. Daviaud, M. Faury, V. Berger
- **CNRS INP & DAS :** E. Lacaze, E. Solal, S. Ravy
- **Management :** E. Eliot, G. Chaboussant, A. Menelle, C. Alba-Simionesco, A. Brulet, H. Schober, M. Johnson, J. Estrade, J. Jestin

ANNEX 3

Scientific highlight.
Full text.

nature materials

ARTICLES

https://doi.org/10.1038/s41563-022-01197-2

Check for updates

Disentangling water, ion and polymer dynamics in an anion exchange membrane

Fabrizia Foglia[1]✉, Quentin Berrod[2], Adam J. Clancy[1], Keenan Smith[3], Gérard Gebel[2], Victoria García Sakai[4], Markus Appel[5], Jean-Marc Zanotti[6], Madhusudan Tyagi[7,8], Najet Mahmoudi[4], Thomas S. Miller[3], John R. Varcoe[9], Arun Prakash Periasamy[9], Daniel J. L. Brett[3], Paul R. Shearing[3], Sandrine Lyonnard[2]✉ and Paul F. McMillan[1,10]

Semipermeable polymeric anion exchange membranes are essential for separation, filtration and energy conversion technologies including reverse electrodialysis systems that produce energy from salinity gradients, fuel cells to generate electrical power from the electrochemical reaction between hydrogen and oxygen, and water electrolyser systems that provide H_2 fuel. Anion exchange membrane fuel cells and anion exchange membrane water electrolysers rely on the membrane to transport OH^- ions between the cathode and anode in a process that involves cooperative interactions with H_2O molecules and polymer dynamics. Understanding and controlling the interactions between the relaxation and diffusional processes pose a main scientific and critical membrane design challenge. Here quasi-elastic neutron scattering is applied over a wide range of timescales (10^0–10^3 ps) to disentangle the water, polymer relaxation and OH^- diffusional dynamics in commercially available anion exchange membranes (Fumatech FAD-55) designed for selective anion transport across different technology platforms, using the concept of serial decoupling of relaxation and diffusional processes to analyse the data. Preliminary data are also reported for a laboratory-prepared anion exchange membrane especially designed for fuel cell applications.

There is a growing need to develop efficient energy conversion devices using sustainable fuel sources[1–5]. Polymer electrolyte membrane (PEM) fuel cells (FCs) that rely on a hydrophobic backbone decorated with ionic side groups to allow selective transport of H^+ or OH^- are one promising technology. The transport mechanisms involve cooperative interactions between the ions, H_2O molecules in the surrounding environment and relaxation dynamics of the polymer backbone and side groups. Established FCs employ electrocatalytic reduction of H_2 to generate H^+ ions that are transported through the PEM, but they rely on Pt-group-metal-based catalytic nanoparticles to effect the kinetically hindered cathodic oxygen reduction reaction as well as H_2 oxidation. Efforts are underway to develop anion exchange membrane (AEM) systems that employ more-sustainable non-noble-metal electrocatalysts[6]. These require efficient OH^- conducting membranes that can withstand highly alkaline operating environments.

Proton-conducting PEMs derived from Nafion (sulfonated tetrafluoroethylene-based fluoropolymer copolymers) are widely implemented in current FCs and water electrolyser systems (WEs). Anion-conducting membranes are less well developed but available as specialty products from companies such as Fumatech[7]. New AEMs incorporating polymer backbones functionalized with quaternary ammonium (QA), imidazolium or guanidinium cations are under development[3,8–11]. The number of water molecules per ionic head group (λ)[12] is critical in determining the anion conduction mechanism. Simulation studies indicate that ionic current flow in AEMs occurs by a combination of vehicular OH^- diffusion and Grotthuss hopping through the hydrogen-bonded water network solvated by ionomer side groups (Fig. 1b–d)[13–19]. Changes in water content under operational conditions affect both H_2O and OH^- mobility, and these are both affected by the molecular architecture of membrane ion-conducting channels[16–18,20–22]. The water, ion and polymer dynamics are strongly coupled on picosecond to nanosecond timescales over spatial correlations up to several nanometres. It is essential to determine the molecular-to-mesoscale transport mechanisms of OH^- in relation to membrane hydration and polymer relaxation dynamics to build the understanding needed for next-generation AEM design.

Quasi-elastic neutron scattering (QENS) provides a powerful technique to study these processes, with its capacity to combine selective chemical and isotopic substitutions using data obtained from instruments with access to different energy ranges to disentangle various dynamical contributions across picosecond–nanosecond timescales. Nafion membranes and related model systems have been probed extensively using QENS[23–26]. The Fumasep FA series of membranes is marketed for anion conduction[27–31]. Fumasep FAD-55, studied here, is a non-reinforced AEM with high electronic and low ionic resistance, stable in alkaline environments up to pH 9 (ref. [27]). Previous QENS investigations on related FAA-3 membranes could not establish the OH^- hopping process nor its correlation with water content and polymer dynamics[32,33]. We present a detailed analysis of QENS data for FAD-55 (refs. [27–30]) in its

[1]Department of Chemistry, Christopher Ingold Laboratory, University College London, London, UK. [2]Université Grenoble Alpes, CNRS, CEA, IRIG-SyMMES, Grenoble, France. [3]Electrochemical Innovation Lab, Department of Chemical Engineering, University College London, London, UK. [4]ISIS Neutron and Muon Source, Science & Technology Facilities Council, Rutherford Appleton Laboratory, Harwell Science and Innovation Campus, Chilton, UK. [5]Institut Laue Langevin, Grenoble, France. [6]Laboratoire Léon Brillouin (CEA-CNRS), Université Paris-Saclay, CEA Saclay, Gif-sur-Yvette Cedex, France. [7]NIST Center for Neutron Research (NCNR), National Institute of Standards and Technology, Gaithersburg, MD, USA. [8]Department of Materials Science and Engineering, University of Maryland, College Park, MD, USA. [9]Department of Chemistry, University of Surrey, Guildford, UK. [10]Deceased: Paul F. McMillan. ✉e-mail: f.foglia@ucl.ac.uk; sandrine.lyonnard@cea.fr

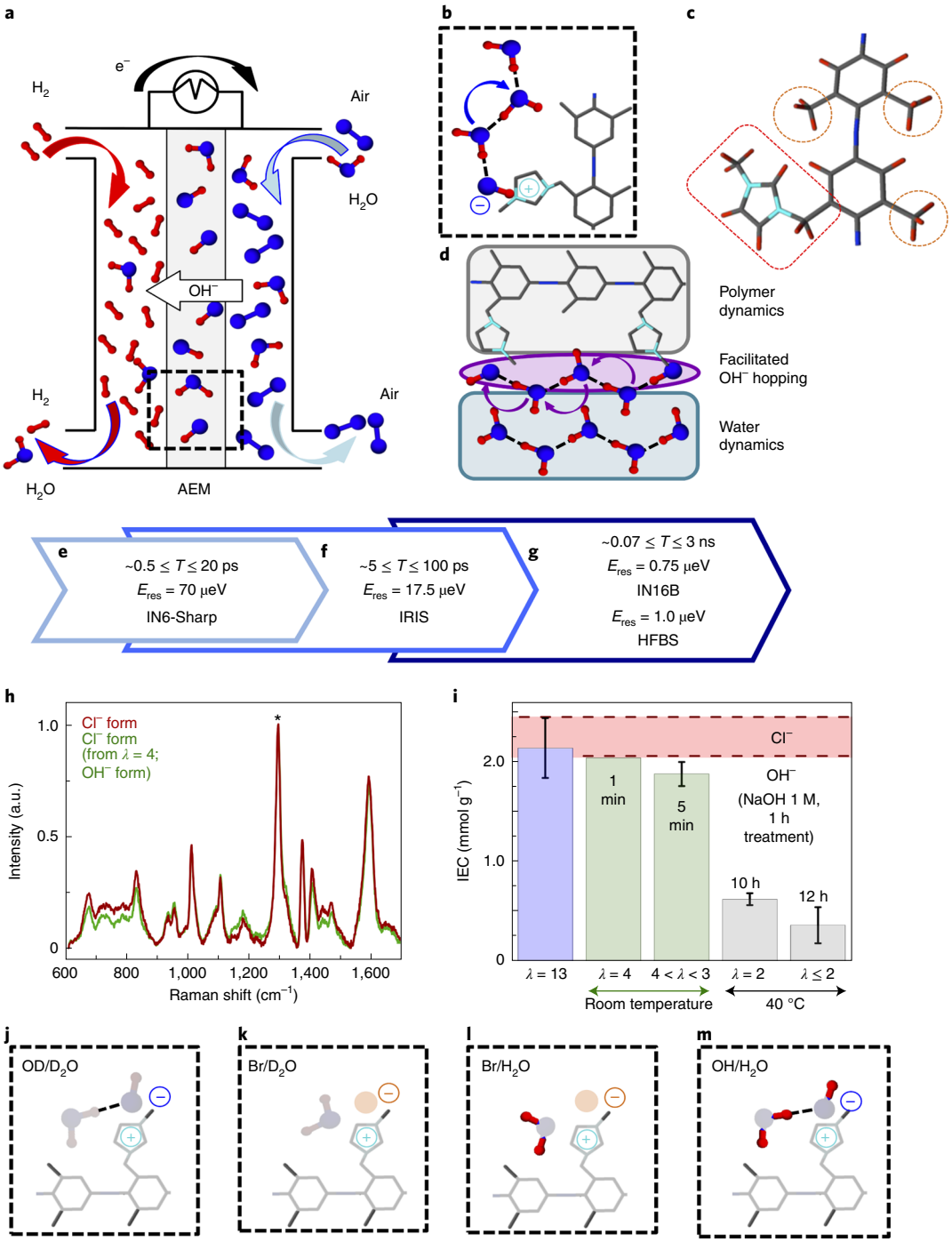

Fig. 1 | Schematic illustration of AEM-FC and the FAD-55 AEM in relation to measurement protocol. a, Schematic illustration of an AEM-FC and its mode of operation. The dashed black box corresponds to the box shown in **b**. e⁻, electron. **b**–**d**, Sketches illustrating the polymeric membrane, the facilitated OH^- hopping mechanism and water translational dynamics and interactions between these dynamic processes. The cartoon in **c** shows rapidly relaxing $-CH_3$ species attached to the polymer backbone[9] and functional groups[8–10,35]. Here we have presumed a structural model for the side-group functional groups based on our Raman spectroscopic analyses[35]. **e**–**g**, Timescales probed in neutron scattering experiments at instruments with different energy resolution characteristics. **h**, Raman spectra recorded on a sample of FAD in its Cl-form (red spectrum, where the FAD sample had not been exposed to any high-pH or low-hydration conditions) and a sample in the Cl-form after it had been dehydrated at $\lambda = 4$ in the OH-form (green spectrum); spectral intensities are normalized to the peak labelled * to aid in visual comparison. **i**, IEC values for Cl-form FAD samples after they had been treated to different hydration states in the OH-form (green and grey bars; dehydrated at room temperature and 40 °C, respectively) compared to its Cl-form (pristine; brown dotted range). **j**–**m**, Chemically and isotopically substituted AEM and hydration medium combinations used to investigate different aspects of the dynamics.

as-supplied Br- as well as OH/OD- and Cl-substituted forms, over a range of temperatures and hydration levels, using different neutron spectrometers to probe the relaxation and transport dynamics over a wide range of timescales, and disentangle details of the correlated polymer–water interactions and OH^--conductivity mechanism (Fig. 1e–g). The QENS studies are complemented by investigation

of the polymer degradation occurring when handling OH-forms of the membrane, along with the determination of the anionic conductivity correlated with the QENS results. Complementary QENS data were also obtained for a new laboratory-prepared membrane specifically targeted at AEM-FC applications (Supplementary Fig. 8)[34].

Samples and measurement conditions

To evaluate the effects of membrane swelling and water content on the ion mobility, membranes were examined in partially to fully hydrated states expressed in terms of λ to highlight and interpret effects occurring at the molecular scale to the nanoscale, while compensating for ionic exchange capacity (IEC) effects and differences in macroscopic water uptake by different membrane formulations and treatments (Supplementary Information).

AEMs are susceptible to degradation of the functional groups attached to the polymer backbone in high-pH environments, especially at low λ values and high temperatures[10,22]. We tested the membrane stability of FAD samples handled under different hydration and thermal conditions in the OH-form by examining the IEC and vibrational (Raman and infrared) spectra (Fig. 1h,i). The data were collected on the samples after reconversion back to the Cl-form after initial handling in the OH-form, and comparing to a Cl-sample that was not treated with any alkali. We combined our H_2O content determined by thermogravimetric analysis (TGA) constrained by the degradation studies and the IEC results to determine the λ values of different hydrated membranes. We saw no substantial degradation (<20%; Supplementary Fig. 2) when FAD was handled in its OH-form at $\lambda > 3$ at room temperature, as indicated by the relative intensities of the Raman peaks at 1,018 and 1,412 cm^{-1} due to *N*-methylimidazolium side groups[35]. These λ values correspond to operational hydration levels achieved within AEM-FCs that are not operating at high current densities (Supplementary Fig. 1h–I and Supplementary Text 1)[36]. We did not observe any notable carbonation occurring during sample preparation for QENS studies (Supplementary Fig. 4), nor any modification of QENS profiles before temperature, *T*, scans in the range 2–325 K (Supplementary Fig. 16a–e).

Notable degradation (>70%; Supplementary Text 1) occurs only after prolonged (≥10 h) treatment under harsh alkaline conditions for dehydrated membranes at ≥40 °C. After treatment under these conditiitions ($\lambda = 2$), TGA results for the degraded membrane indicated a ~2 wt% weight loss below 400 K corresponding to two water molecules that remained strongly hydrogen bonded to the OH^- group in the nominally dried sample, providing insight into understanding the OH^- transport mechanism in intact OH-membranes at higher λ values, discussed below (Supplementary Fig. 1). Weight losses observed at higher *T* are associated with thermal degradation of the QA groups and polymer backbone[37].

Chemically and isotopically substituted versions of FAD-55 and its hydrating medium were examined: (1) the sample in its as-supplied Br-form hydrated in either D_2O or H_2O; (2) the membrane in OH-form hydrated in H_2O; and (3) the AEM sample in OD-form hydrated in D_2O (Supplementary Fig. 1j–m). The fully deuterated contrast (OD/D_2O) was designed to focus on polymer backbone relaxation, including QA methyl side-group rotation (Fig. 1c). The fully hydrogenated sample (OH/H_2O) targeted water- (at $\lambda = 13$) and OH^--facilitated hopping dynamics that were revealed at high-energy resolution. Comparisons with the Br/D_2O and Br/H_2O data allowed us to evaluate the potential effects of OH^- nucleophilic attack on the QA side groups, which are considered to be a primary cause of degradation in AEM performance, especially at low hydration[3,10,21,38]. A newly prepared AEM of high-density polyethylene radiation-grafted with vinylbenzyl chloride aminated with trimethylamine (HDPE-VBC-TMA)[34] was also examined at $\lambda = 4$ in OH/H_2O (Supplementary Fig. 8), focusing on high-resolution experiments (via the backscattering spectrometer IN16B) to directly show the facilitated OH^- hopping mechanism observed for FAD. Samples had been previously tested for water uptake as well as for alkaline resistance, with IEC decreases of <10% when the membrane is dehydrated to $\lambda = 4$ in OH-form[34]. Preliminary results are presented here for comparison with the FAD-55 data; a detailed analysis of the dynamical properties of this new membrane will be reported elsewhere (Foglia, F. et al. (in preparation)). Neutron scattering experiments were performed at different instruments with complementary energy resolutions (E_{res}) to disentangle the interacting contributions to the polymer, H_2O and OH^- dynamics. The facilities were as follows: the ISIS Neutron and Muon Spallation Source (ISIS; Harwell, UK); the Institut Laue Langevin (ILL; Grenoble, France); and the National Institute of Standards and Technology (NIST) Center for Neutron Research (Gaithersburg, MD, USA). The instruments used were (1) the high-resolution backscattering spectrometers IN16B (ILL) and High Flux Backscattering Spectrometer (HFBS; NIST), with E_{res} of 0.75 and 1 μeV, respectively (~0.07–3 ns); (2) the time-of-flight (TOF) near-backscattering spectrometer IRIS (ISIS; $E_{res} = 17.5$ μeV; ~5–100 ps); and (3) the IN6-Sharp (operated by the Laboratoire Léon Brillouin at ILL) TOF spectrometer ($E_{res} = 70$ μeV; ~0.5–20 ps; Fig. 1e–g).

Different dynamic regimes revealed by fixed window scans

Elastic and inelastic scattering intensities were analysed using fixed window scans (EFWS and IFWS, respectively) by increasing (IN16B, HFBS, IN6-Sharp) or lowering (IRIS) the temperature (*T*) between 2 and 325 K. EFWS data and mean square atomic displacement (m.s.d.) values extracted by Debye–Waller analysis are shown in Fig. 2, with complementary IFWS data provided in the Supplementary Information, giving insight into the sequential activation of different dynamical processes as a function of *T*. As each process (*i*) becomes activated at T_i, the elastic intensity drops, accompanied by a corresponding increase in inelastic intensity, so that the onset of different dynamic processes is revealed by slope changes in the EFWS and IFWS intensity profiles. These EFWS/IFWS variations are modulated by the finite energy or timescale resolution available to each spectrometer, with the dynamics becoming either too fast or too slow compared with the observational window. Analysis of the datasets obtained across the different instruments thus permits recognition of different dynamic regimes and relaxation behaviours as a function of temperature across all AEM samples and hydration states (Fig. 2).

Region 1 in Fig. 2 (<200 K) is characterized by a regular loss in EFWS intensity, accompanied by an m.s.d. increase of up to ~200 K, with average slope $d\langle u^2\rangle/dT \approx 7.4 \pm 0.8 \times 10^{-4}$ $Å^2 K^{-1}$ (where u^2 is the mean square displacement) for $\lambda = 4$ (IN16B, HFBS, IRIS), increasing to $13.4 \pm 0.2 \times 10^{-4}$ $Å^2 K^{-1}$ when examined within the fast (0.5–20 ps) timescale window of IN6-Sharp. We assign these effects excited at low temperature to fast rotations of $-CH_3$ groups attached to the polymer[39]. The larger m.s.d. change recorded at IN6-Sharp occurs as additional large-amplitude and acoustic-type motions of the polymer backbone contribute to the excitation profile.

In region 2 (>200 K), we observe a rapid EFWS decrease accompanied by a sharp m.s.d. rise for H_2O-hydrated samples ($\lambda = 4$; Fig. 2a), along with an IFWS intensity maximum recorded at IN16B (Supplementary Fig. 5). This apparent maximum arises as the probed dynamics enter the backscattering window at ~200 K, to reach an energy-dependent maximum at ~260 K, and then vanish at higher *T* as the motional timescales become faster than the observational window. The relaxation time (τ) for this feature is independent of the scattering correlation length (*Q*), indicating a spatially localized process, as is found for the $-CH_3$ rotational excitations discussed above, but on a slower timescale. Because analogous behaviour is observed for different AEM hydration levels as well as for the OH/H_2O and Br/D_2O samples, we can assign these additional features to the activation of fast polymer side-chain dynamics, occurring on a timescale of a few picoseconds.

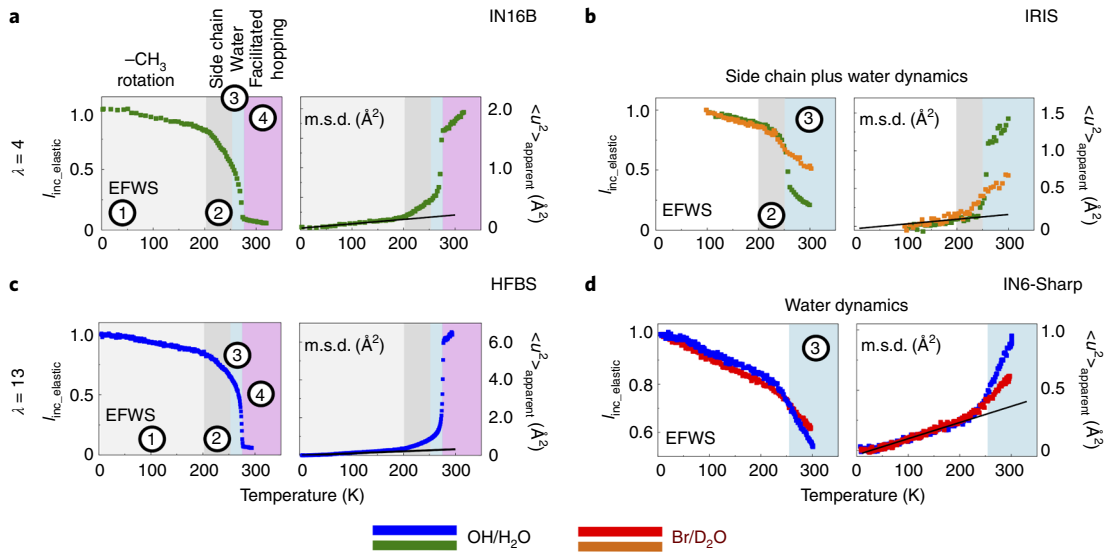

Fig. 2 | EFWS intensity and m.s.d. data for FAD-55 membrane. Profiles were recorded for FAD-55 at different hydration levels ($\lambda = 4$, 13) and isotopic compositions (OH/H_2O and Br/D_2O) at instruments with different E_{res} values. The datasets are separated according to hydration level. **a**,**b**, Low-hydration samples ($\lambda = 4$). **c**,**d**, Fully hydrated samples ($\lambda = 13$). Data obtained at each instrument are in different panels: 0.75 μeV (**a**; high-resolution IN16B); 1.0 μeV (**c**; high-resolution HFBS); 17.5 μeV (**b**; intermediate-resolution IRIS); and 70 μeV (**d**; broad-resolution IN6-Sharp). The OH/H_2O-hydrated samples (for example, the OH-form) are reported as blue ($\lambda = 13$) and green ($\lambda = 4$) symbols; the Br/D_2O-hydrated samples (for example, the Br-form) are designated by red ($\lambda = 13$) and orange ($\lambda = 4$) symbols. Information extracted on m.s.d. values is provided at the right in each panel. The m.s.d. slope extrapolated from the data at low-T is shown as a black line. The plots are used to highlight four dynamic ranges of interest: (1) $-CH_3$ polymer dynamics, (2) side-chain polymer dynamics, (3) water dynamics and (4) facilitated ion hopping. $I_{inc\_elastic}$, elastic intensity; $\langle u^2_{apparent}\rangle$, apparent mean square displacement. Corresponding IFWS data and analysis details are provided in the Supplementary Information.

Region 3 is recognized by a sudden drop in EFWS intensity beginning at 250 K, clearly visible across the entire range of slower (IN16B, HFBS; Fig. 2a,c), intermediate (IRIS; Fig. 2b) and fast (IN6-Sharp; Fig. 2d) timescale measurements. The activated process shows a Q-dependency at low-Q, indicating a contribution from centre-of-mass mobility of the species involved. The EFWS changes are more pronounced for H_2O-hydrated than for D_2O-hydrated samples (Fig. 2b), with the number of mobile species proportional to the hydration state. An accompanying increase in IFWS intensity above 250 K is likewise dependent on the hydration state and isotopic composition (Supplementary Information). We assign this additional Q-dependent process to rotational–translational water dynamics activated within hydrated AEM samples.

Region 4 is first observed as a moderate but regular decrease in EFWS intensity for the $\lambda = 4$ sample measured on IN16B above $T \approx 270$ K, accompanied by a continued m.s.d. increase with reduced slope (Fig. 2a). Similar changes are observed for $\lambda = 13$ at HFBS (Fig. 2c). These observations indicate activation of a further dynamic process occurring on a much slower timescale than those described above. The IFWS signal is Q-invariant (Supplementary Fig. 5), indicating localized dynamics. We assign this additional process to ion hopping facilitated by the remaining H_2O molecule bridging two OH^- groups, revealed by TGA. It is clearly detectable only on high-resolution spectrometers; although both polymer motions and roto-translational water dynamics remain active, these have become too fast to be observed as discrete contributions to the EFWS and IFWS within the resolution window available to lower-resolution instruments.

Relaxation processes revealed by QENS analysis

We analysed QENS contributions to datasets plotted in the energy domain between 230 and 325 K and $4 \leq \lambda \leq 13$ by fitting Lorentzian functions guided by the EFWS, m.s.d. and IFWS results described above (Fig. 3; analysis details in Supplementary Information). We first describe the fast (1–4 ps) Q-independent polymer backbone and side-chain dynamics for samples containing no mobile protons in the ionic phase (D_2O-hydrated samples on IRIS and IN6-Sharp[40]; Fig. 3a–d). These localized dynamics, present above 230 K with an activation energy $E_{A\_polymer} \approx 6.3$ kJ mol^{-1}, display a decrease in $\tau_{polymer}$ with increasing temperature, with an enhanced slope for higher hydration levels (Fig. 3c,d). Because these dynamics are present for all samples, this contribution was constrained to be a common component for all the analyses.

In high-resolution (for example, IN16B, with $E_{res} = 0.75$ μeV) datasets, this contributes to a broad underlying QENS background (that is, polymer dynamics as detected on IRIS and IN6-Sharp and present at all λ and T values; Supplementary Text 2.2). Water relaxations also contribute to this broad signal. However, the most important feature is the presence of a Q-independent Lorentzian signal of much smaller width (a few microelectronvolts, equivalent to ~270 ps). The origin of this component was identified by comparing OH- and Br-datasets (Supplementary Text 2.2) and assigned to slow OH^- hopping dynamics assisted by H_2O molecules bridging two OH^- (Fig. 3e–i)[17]. This latter contribution was first detected for $\lambda = 4$ samples at lower temperature (230 K; Fig. 3f), and was maintained at higher hydration levels where the broad background contained contributions from both polymer and H_2O relaxations (Fig. 3f,g). The OH^- residence time ($\tau_{hopping}$) and mean hopping distance (2σ) were determined from the Q-independent QENS half-width at half-maximum ($\tau_{hopping} = \hbar/\Gamma$, where $\hbar$ is the reduced Planck's constant and Γ is the half-width at half-maximum) and intensity ($I = (1 - \exp(-Q^2\sigma^2))$; Fig. 3h,i (ref. [24])).

Analysis of the data indicated a pronounced T dependency between 230 and 325 K with an average activation energy $E_A = 4.0 \pm 0.2$ kJ mol^{-1} (depending on the hydration state) accompanied by an increase of the hopping distance 2σ between 1.8 and 2.8 Å (Fig. 3h,i). Increasing hydration from $\lambda = 4$ to 13 led to a reduction in $\tau_{hopping}$ between 270 and 200 ps, associated with longer (2.5 Å

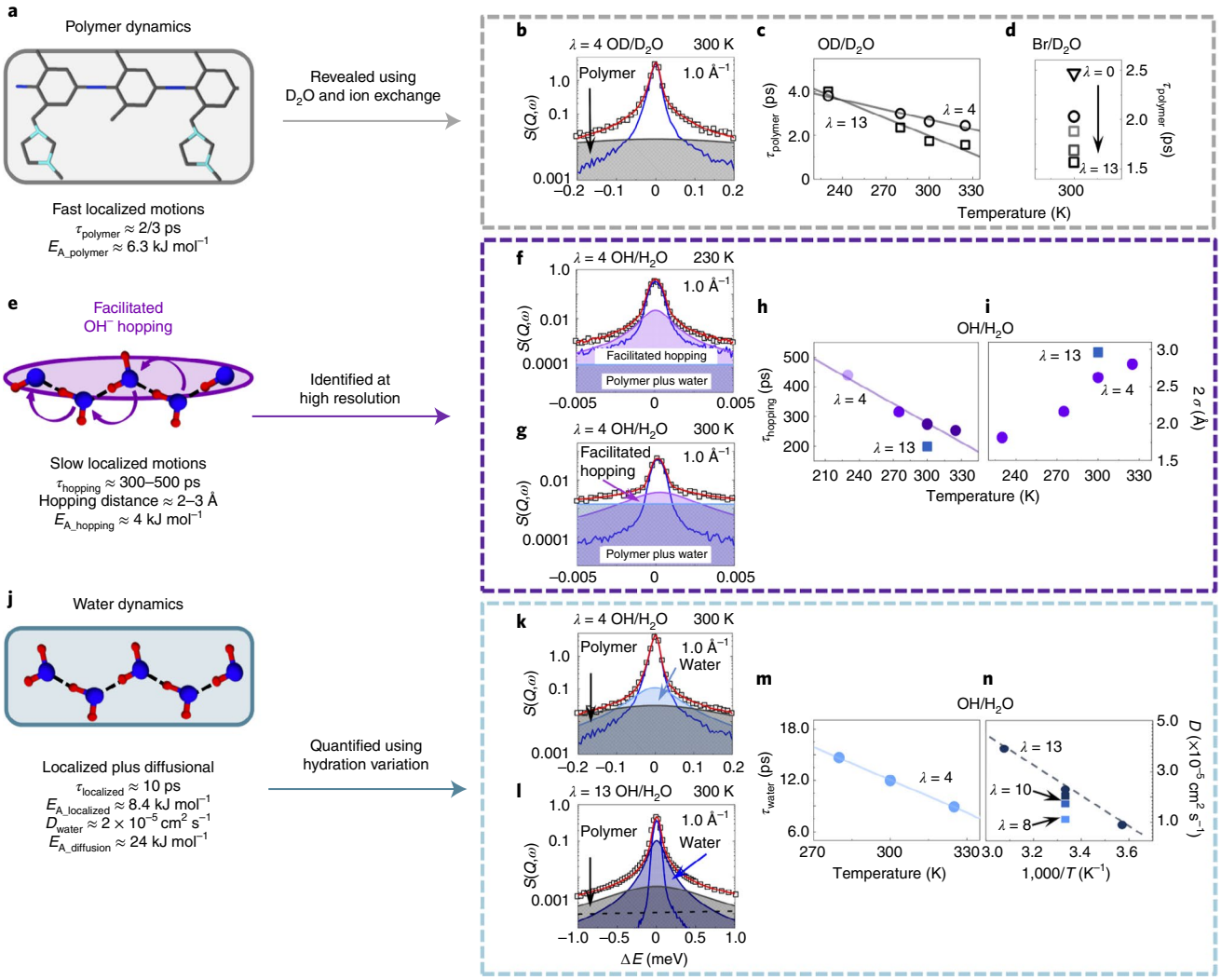

Fig. 3 | Analysis of QENS associated with different dynamical processes; data for FAD-55 membrane. a, Schematic illustration of polymer dynamics incorporating methyl group pseudorotation and other fast (1–4 ps, depending on hydration state) side-chain and backbone dynamics activated above $T \approx 230$ K. **b**, Analysis of the signal obtained at $T = 300$ K for a $\lambda = 4$ OD/D_2O sample using $E_{res} = 17.5$ μeV (intermediate resolution, IRIS). The instrument resolution function is shown as a solid blue line underneath the data points (open squares). The fast polymer relaxation gives rise to an extremely broad Lorentzian contribution (grey shaded area) underlying the data. The convolution of the two is shown as the red line fitting through the data points. **c**, Relaxation times ($\tau_{polymer}$) for the polymer dynamics extracted from the QENS line-widths for OD/D_2O samples with different hydration levels ($\lambda = 4$–13) between $T = 230$ K and $T = 325$ K. **d**, The $\tau_{polymer}$ values determined for Br/D_2O samples at 300 K as a function of hydration level ($\lambda = 0$–13). **e**, Schematic illustration of slow (200–500 ps) facilitated OH^- ion hopping dynamics that can be mediated by either vehicular transport of OH^- ions or Grotthuss H^+ transport, depending on the hydration level of the AEM. **f**,**g**, Scattering profiles at $\lambda = 4$ for OH/H_2O samples at 230 and 300 K, respectively, measured at IN16B (high resolution). The narrow Lorentzian signal (mauve shaded area) represents the facilitated OH^- hopping dynamics superimposed on a very broad background (light blue) corresponding to underlying polymer plus water dynamics, which occur on timescales that are too rapid to contribute to the narrower Lorentzian function within the instrumental E_{res} (0.75 μeV). Symbols and lines for the experimental data (squares), instrumental resolution function (blue lines) and global fit (red lines) are as in **b**. **h**, Facilitated hopping dynamics timescale ($\tau_{hopping}$) extracted from QENS line-widths as a function of temperature ($230 \leq T \leq 325$ K) for OH/H_2O samples with $4 \leq \lambda \leq 13$. Purple circles, facilitated hopping at $\lambda = 4$ (different shades are made to highlight the T-dependence); blue square, facilitated hopping at $\lambda = 13$; purple line, linear fitting for facilitated hopping at $\lambda = 4$. **i**, OH^- hopping distance (2σ) modelled from QENS data for $4 \leq \lambda \leq 13$ OH/H_2O samples between $230 \leq T \leq 325$ K. Purple circles, hopping distance at $\lambda = 4$; blue square, hopping distance at $\lambda = 13$. **j**, Schematic illustration indicating pseudorotational, diffusional and sometimes nanoconfined dynamics of H_2O molecules occurring within hydrated membrane samples over intermediate (6–14 ps) timescales. **k**,**l**, Scattering profiles for OH/H_2O samples with $\lambda = 4$ and 13, respectively, recorded at 300 K with $E_{res} = 17.5$ μeV (intermediate resolution, IRIS) and 70 μeV (broad resolution, IN6-Sharp), respectively. The water dynamics give rise to the main Lorentzian contribution with narrower line-width (light blue shaded area) with a significantly broader 'background' signal due to polymer relaxations (grey shaded component). **m**, Water relaxation timescale determined from QENS line-widths for $\lambda = 4$ at $230 \leq T \leq 325$ K. Light blue circles, water relaxation at $\lambda = 4$; light blue line, linear fitting for water relaxation at $\lambda = 4$. **n**, Diffusion constants ($cm^2 s^{-1}$) determined from fitting QENS profiles for mobile water molecules within AEM samples with $\lambda = 8$–13, plotted as a function of 1,000/T. Blue circles, diffusion constants for mobile water molecules within AEM samples at $\lambda = 13$ (data aquired on IRIS); black line, linear fitting for diffusion constants for mobile water molecules within AEM samples at $\lambda = 13$ (data aquired on IRIS); blue square, diffusion constants for mobile water molecules within AEM samples with $8 \leq \lambda \leq 13$ (data aquired on IN6-Sharp); different shades highlight the different λ. D, diffusion coefficient; D_{water}, diffusion coefficient for water; ΔE, energy transfer; $E_{A\_hopping}$, activation energy for facilitated hopping process; $E_{A\_localized}$, activation energy for localized dynamics; $E_{A\_diffusion}$, activation energy for diffusive dynamics; $\tau_{localized}$, relaxation time for localized dynamics; τ_{water}, relaxation time for localized dynamics.

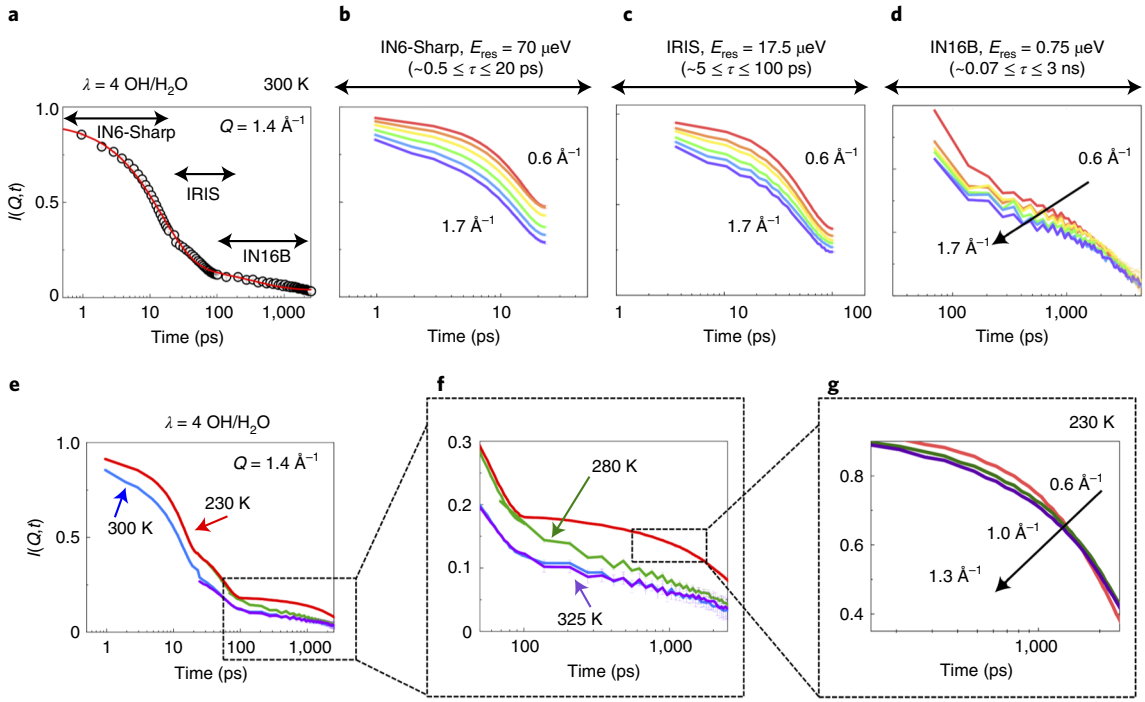

Fig. 4 | Intermediate scattering function to investigate relaxation dynamics as a function of their timescale; data for FAD-55 membrane. a, Scattering profile in the time domain for H_2O-hydrated ($\lambda = 4$) OH-samples, at 300 K and $Q = 1.4$ Å^{-1}. The global fit (red continuous curve) is overlaid across all datasets on the data points (black). **b**–**d**, Q-dependency of $I(Q,t)$ over the investigated timescales. **e**, The temperature dependence for OH-samples that are H_2O hydrated ($\lambda = 4$) between 230 K (red line) and 325 K (purple line); $Q = 1.4$ Å^{-1}. Note here that profiles at 280 K (green line) and 325 K (purple line) have been obtained only at two energy resolutions (IRIS and IN16B). **f**, A highlight of the slow-dynamics process in **e**. **g**, A highlight of **f** showing the deviation from the quadratic dependence of the intermediate scattering function for the OH/H_2O sample at $\lambda = 4$ and $T = 230$ K in the nanosecond timescale. The arrow highlights the Q-dependency (from $Q = 0.6$ Å^{-1} to $Q = 1.3$ Å^{-1}). Full details of the analysis are provided in Supplementary Text 2.5.

versus 3 Å) jump distances (Fig. 3h,i). These results agree with simulations indicating a combination of ballistic, sub-diffusive/rattling and diffusive components of OH^- transport dynamics operating in different but overlapping time regimes[15,19]. The determined values of $\tau_{hopping}$ and 2σ, especially at $\lambda = 4$, indicate that on the IN16B timescale, mainly OH^- 'rattle and hop' events are being probed, with minimal coupling to longer-range molecular/anionic mobility mechanisms[41]. When probed with a faster time window (for example, with IRIS or IN6-Sharp) the facilitated OH^- hopping becomes undetectable, as this component becomes incorporated into the elastic line, while the polymer fast-relaxation component is complemented by a further Lorentzian signal. This new feature is associated with the dynamics of included water molecules (Fig. 3j), and its behaviour evolves as a function of hydration levels. At $\lambda = 4$ (Fig. 3k), it shows Q-independent behaviour, compatible with localized (that is, confined) dynamics ($\tau \approx 10$ ps and $E_A \approx 8.4$ kJ mol^{-1}; Fig. 3m). By $\lambda = 13$ (Fig. 3j), the water dynamics have become Q-dependent, indicating translationally mobile H_2O (Fig. 3n). In all these cases, an additional, approximately linear or extremely broad Lorentzian background was needed to account for very fast (sub-picosecond) relaxations extending from the vibrational regime.

Our QENS analyses correspond to the interpretation of the EFWS/m.s.d./IFWS datasets above by describing separate but coupled dynamical regimes and relaxation phenomena that enter the relaxation profile probed by QENS for isotopically and chemically substituted AEM samples, exposed to H_2O/D_2O solvents, as a function of hydration level and temperature. These include (1) polymer side-chain and backbone dynamics that operate for all samples throughout the temperature range; and (2) localized water motions associated with hydrating H_2O molecules facilitating the release of OH^- ions from active polymer sites[15], combined with (3) bulk-like diffusion and roto-vibrational dynamics of H_2O molecules with a threshold around $\lambda \approx 8$. This progression of water dynamics is rationalized in terms of the activation of diffusive motions as mobility channels increase in size and connectivity. Our data agree with simulations predicting large water clusters that could support confined molecular diffusion above $\lambda = 8$ (ref. [10]). Calculated changes in OH^- diffusivity between $\lambda = 2.5$ and 4 reflect a transition between aqueous clusters where the lack of network connectivity limits long-range diffusion to an enhanced diffusivity regime following the formation of an extended hydrogen-bonded network[42]. Previous QENS analyses of Fumasep FAA showed bulk H_2O diffusion occurring above $\lambda \approx 5$ (refs. [32,33]).

Analysing the $I(Q,t)$ to disentangle different relaxation timescales

The measured scattering datasets $S(Q,\omega)$ (where ω is the energy) were Fourier transformed to obtain the full intermediate scattering function $I(Q,t)$ extending between ~0.5 and 3,000 ps, where t is time (Fig. 4 and Supplementary Text 2.5). This allows an overall view of the sequential processes occurring with different onset temperatures and relaxation dynamics and reveals the coupling between them. This analysis parallels that applied to 'serial decoupling' of relaxational and diffusive modes for glass-forming liquids and ion-conducting polymers[43,44]. The combined $I(Q,t)$ profiles from different instruments reveal clear changes in slope at ~20 and 100 ps, as the dynamic signatures from fast-relaxing polymer motions are followed by H_2O translational and then slower facilitated OH^- hopping processes, which enter the relaxation profile (Fig. 4a and Supplementary Fig. 20). The data for different Q values are shown for the instruments probing different timescale ranges in Fig. 4b–d.

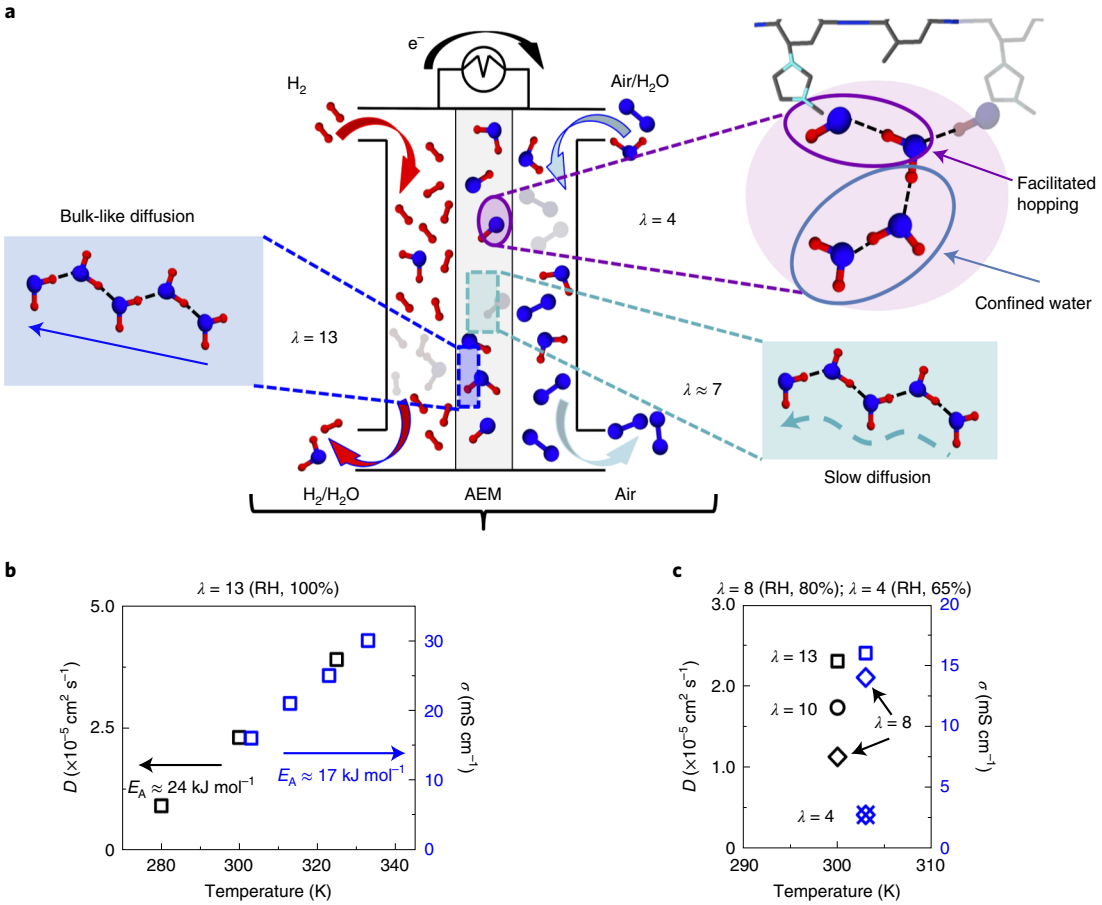

Fig. 5 | From dynamics parameters to AEM performance; data for FAD-55 membrane. a, Schematic illustration of an alkaline FC and its mode of operation. We illustrate key areas of different water uptake with sketches indicating the main modes of OH^-/H_2O transport. At the anode with higher hydration levels (for example, $\lambda = 13$) the transport dynamics are determined by bulk-like water diffusion, whereas the lower hydration (for example, $\lambda = 4$, which can drop to $\lambda = 1$ at high current densities) at the cathode involves OH^- hopping facilitated by the presence of H_2O molecules hydrogen-bonded to the OH^- groups attached to ionomer QA side groups. Within the membrane, the faster anionic diffusion within the aqueous component at intermediate hydration (for example, $\lambda = 8$) is slowed by interaction with the polymer. **b**,**c**, Comparison between diffusion coefficient of anionic species, determined from QENS results (black symbols, left axis) and measured ionic conductance (blue symbols, right axis). Data are shown for $\lambda = 13$ (square symbols in **b** and **c**), as well as for $\lambda = 10$, 8 and 4 (circle, diamond and crossed diamond, respectively in **c**). In **b** and **c**, black (left) labels refer to diffusion coefficient (D in $cm^2\,s^{-1}$; black symbols), and blue (right) labels refer to OH^- conductivity (σ in $mS\,cm^{-1}$; blue symbols). RH, relative humidity.

Focusing on the $\lambda = 4$ sample studied at 230 K, the scattering function first develops a plateau at ~100 ps followed by a shallower $I(Q,t)$ reduction at longer timescales (Fig. 4e,f). This sample exhibits a change in Q-dependency at slow timescales with an inflection at ~2,000 ps (0.6–1.3 $Å^{-1}$; Fig. 4g), revealing 'rattling' motions over nearest neighbour (~3 Å) distances. The results indicate species localized within cage sites, which could have the ability to diffuse over longer (that is, exceeding the probed window) timescales[45]. Above 280 K, the plateau almost disappears (Fig. 4f) and the entire curve shifts towards shorter timescales (Fig. 4e). The transition between the two behaviours (278 K) sets a limit between facilitated hopping versus diffusion processes controlling the transport and thus dominating the scattering profile, as found for supercooled liquids[46].

The data also highlight an additional underlying component that enhances the facilitated hopping mechanism and eventually dominates the scattering profile above 280 K. This component, visible on the IRIS timescale (Supplementary Fig. 12), could be responsible for the IFWS Q-dependence at very low-Q (Supplementary Figs. 5 and 6). It might well result from interconnectivity developed between water domains[47] and formation of a hydrogen-bonded network, both of which are essential for efficient FC operation[42]. Under fully hydrated conditions, diffusive transport begins to dominate the coupled process, as evidenced by the Q-dependence of $I(Q,t)$ at faster timescales (Supplementary Fig. 20). The implementation of the timescale decoupling approach further permits the identification of a long-range component around one order of magnitude slower that leads to the $I(Q,t)$ decay observed, into the nanosecond regime, as well as to the quantification of fast versus slow mobile fractions. The 'slow' population includes counting two protons per dynamic event, due to one water molecule bridging between QA polymer side groups and facilitating the OH^- hopping mechanism (Fig. 5a).

Relationships of nanoscale dynamics to OH^- conductivity

We measured ionic conductance for FAD in different ionic forms to compare with our QENS analysis (Fig. 5 and Supplementary Fig. 3). A main factor determining anionic mobility concerns the structural integrity of the polymer backbone and ionomeric side groups under the highly alkaline conditions and elevated temperatures during operation. Our degradation studies indicate that FAD-55 maintains its polymeric and side-chain structure at $T < 40\,°C$ under alkaline conditions for $\lambda = 4$ and above. AEM-FCs are expected to function at higher temperature (>60 °C and up to 80–95 °C), for which

more pH- and T-resistant membranes are now being designed and tested[48]. FAD-55 exhibited a noticeable loss in conductivity when operated under low-hydration ($\lambda = 4$) and high-T (>40 °C) conditions, as expected from the degradation results.

The anionic conductivity is also known to be affected by the potential reaction of the OH^- groups with atmospheric or dissolved CO_2, causing the formation of (bi)carbonate species, especially under low-hydration conditions[49,50]. We carefully excluded CO_2 from the sample chambers for our QENS experiments, and Fourier transform infrared spectroscopy data taken for samples following similar preparation and analysis protocols showed no evidence of these species (Supplementary Fig. 4). Our conductivity results found the OH^- mobility to be approximately twice that of Cl^- (Supplementary Fig. 3).

The degree of water uptake controls the delicate balance between vehicular versus hopping transport mechanisms, as discussed above[17,47]. Computational studies show that as a consequence of electro-osmotic drag, water is partitioned unevenly within the cell along the trajectory between the cathode and anode (Fig. 5a)[51]. Under fully hydrated conditions, the coupled process is dominated by vehicular transport with a D_{tr} value (where D_{tr} is the self-diffusion coefficient for translationally mobile species) comparable to the total diffusion coefficient for membranes similar to FAD[15–18]. The simulations further indicate a long-range component comparable to the value computed for OH^- diffusion[15,16], suggesting that the Grotthuss mechanism contributes ~15% to the total process.

The activation energy $E_A = 24.5 \pm 4.5\,kJ\,mol^{-1}$ for coupled OH^-/H_2O diffusion determined by QENS is comparable with that from conductance ($17.3 \pm 0.1\,kJ\,mol^{-1}$; Fig. 5b). The higher conductivity is related to the different effect of the hydration shell around the anions, with hydrogen bonding between OH^- and H_2O facilitating diffusion and proton hopping. As the hydration level is lowered to $\lambda = 8$, representing a typical overall water content within an AEM polymer matrix under normal operating conditions[51], the self-diffusion coefficient becomes ~50% slower than at $\lambda = 13$ (Fig. 5c). A smaller (~10%) conductivity variation is found when comparing with operation at similar temperatures (Fig. 5c). This result suggests that vehicular transport provides the main contribution to the anion conductivity at high hydration levels. Above $\lambda = 8$ we expect that channels with bulk water facilitate vehicular diffusion of the anions. At $\lambda = 4$ and below, water-mediated OH^- hopping becomes the primary component of the coupled transport mechanism, with a limited contribution from vehicular transport activated above 280 K, as demonstrated by the IRIS QENS datasets and the $I(Q,t)$ values observed at fast timescales (Fig. 4e,f), as well as by the remarkable reduction in conductivity by around one order of magnitude (Fig. 5c). This reduction cannot be ascribed to membrane degradation, as complete recovery of the conductivity is observed at 303 K (Supplementary Fig. 3b); it is, therefore, due to suppression of ion structural diffusion as well as a lower degree of dissociation (as observed in proton-conducting materials).

Our results indicate that OH^- transport via Grotthuss H^+ hopping is enabled within a dynamic complex with three 'fast' and one 'slow' H_2O molecules bridging two OH^- groups, corresponding to the structural configuration suggested for the strongly bound remnant water found by TGA for our fully dried 'reference' sample. These three H-containing species must be doubled in number to activate the complementary mass transport process. Our diffusion results at low hydration, where OH^- has only its first hydration shell completed, are consistent with the model proposed by Zelovich et al.[19].

Conclusions

Our results provide insights into OH^- transport dynamics relevant to the operation of AEM-FCs and other devices. They support previous simulations indicating that charge transport occurs by a combination of vehicular OH^- diffusion and Grotthuss H^+ exchange, with the two mechanisms balanced according to the hydration level[13–18,52]. The reduced efficiency of anion transport at low hydration is due to the absence of the coupling with H_2O diffusional dynamics that is enabled at higher hydration, rather than degradation of ionomer functionality. The fact that the dynamics are associated with two slow protons, indicating the need for one H_2O molecule to mediate the OH^- transport, explains why the slower vehicular mechanism dominates at low hydration. At medium hydration, the conductivity is determined by the water mobility slowdown through interactions with the polymer matrix, whereas at high hydration, the diffusivity is dominated by bulk water dynamics. The insights provided by these data provide a guide for the design of new devices, where tuning the membrane nanostructure would result in activation of the anionic hopping mechanism, providing improved performance over a wide range of operational conditions.

Online content

Any methods, additional references, Nature Research reporting summaries, source data, extended data, supplementary information, acknowledgements, peer review information; details of author contributions and competing interests; and statements of data and code availability are available at https://doi.org/10.1038/s41563-022-01197-2.

Received: 11 November 2020; Accepted: 11 January 2022;
Published online: 17 March 2022

References

1. Zlotorowicz, A., Strand, R. V., Burheim, O. S., Wilhelmsen, Ø. & Kjelstrup, S. The permselectivity and water transference number of ion exchange membranes in reverse electrodialysis. *J. Membr. Sci.* **523**, 402–408 (2017).
2. Gottesfeld, S. et al. Anion exchange membrane fuel cells: current status and remaining challenges. *J. Power Sources* **375**, 170–184 (2018).
3. Varcoe, J. R. et al. Anion-exchange membranes in electrochemical energy systems. *Energy Environ. Sci.* **7**, 3135–3191 (2014).
4. Kumar, S. S. & Himabindu, V. Hydrogen production by PEM water electrolysis—a review. *Mater. Sci. Energy Technol.* **2**, 442–454 (2019).
5. Henkensmeier, D. et al. Overview: state-of-the art commercial membranes for anion exchange membrane water electrolysis. *J. Electrochem. Energy Convers. Stor.* **18**, 024001 (2021).
6. Hren, M., Božič, M., Fakin, D., Kleinschek, K. S. & Gorgieva, S. Alkaline membrane fuel cells: anion exchange membranes and fuels. *Sustain. Energy Fuel* **5**, 604–637 (2021).
7. FuelCellStore. Fumasep FAD-55 https://www.fuelcellstore.com/fuel-cell-components/membranes (2020).
8. Barnes, A. M., Liu, B. & Buratto, S. K. Humidity-dependent surface structure and hydroxide conductance of a model quaternary ammonium anion exchange membrane. *Langmuir* **35**, 14188–14193 (2019).
9. Ran, J. et al. Anion exchange membranes (AEMs) based on poly(2,6-dimethyl-1,4-phenylene oxide) (PPO) and its derivatives. *Polym. Chem.* **6**, 5809–5826 (2015).
10. Pusara, S., Srebnik, S. & Dekel, D. R. Molecular simulation of quaternary ammonium solutions at low hydration levels. *J. Phys. Chem. C* **122**, 11204–11213 (2018).
11. Ramaswamy, N. & Mukerjee, S. Alkaline anion-exchange membrane fuel cells: challenges in electrocatalysis and interfacial charge transfer. *Chem. Rev.* **119**, 11945–11979 (2019).
12. Springer, T. E., Zawodzinski, T. A. & Gottesfeld, S. Polymer electrolyte fuel cell model. *J. Electrochem. Soc.* **138**, 2334–2342 (1919).
13. Marx, D., Chandra, A. & Tuckerman, M. E. Aqueous basic solutions: hydroxide solvation, structural diffusion, and comparison to the hydrated proton. *Chem. Rev.* **110**, 2174–2216 (2010).
14. Tuckerman, M. E., Marx, D. & Parrinello, M. The nature and transport mechanism of hydrated hydroxide ions in aqueous solution. *Nature* **417**, 925–929 (2002).
15. Dubey, V., Maiti, A. & Daschakraborty, S. Predicting the solvation structure and vehicular diffusion of hydroxide ion in an anion exchange membrane using nonreactive molecular dynamics simulation. *Chem. Phys. Lett.* **755**, 137802 (2020).
16. Chen, C., Tse, Y.-L. S., Lindberg, G. E., Knight, C. & Voth, G. A. Hydroxide solvation and transport in anion exchange membranes. *J. Am. Chem. Soc.* **138**, 991–1000 (2016).

17. Dong, D., Zhang, W., van Duin, A. C. T. & Bedrov, D. Grotthuss versus vehicular transport of hydroxide in anion-exchange membranes: insight from combined reactive and nonreactive molecular simulations. *J. Phys. Chem. Lett.* **9**, 825–829 (2018).
18. Zhang, W., Dong, D., Bedrov, D. & van Duin, A. C. T. Hydroxide transport and chemical degradation in anion exchange membranes: a combined reactive and non-reactive molecular simulation study. *J. Mater. Chem. A* **7**, 5442–5452 (2019).
19. Zelovich, T. et al. Hydroxide ion diffusion in anion-exchange membranes at low hydration: insights from ab initio molecular dynamics. *Chem. Mater.* **31**, 5778–5787 (2019).
20. Li, X., Yu, Y., Liu, Q. & Meng, Y. Synthesis and characterization of anion exchange membranes based on poly(arylene ether sulfone)s containing various cations functioned tetraphenyl methane moieties. *Int. J. Hydrog. Energy* **38**, 11067–11073 (2013).
21. Diesendruck, C. E. & Dekel, D. R. Water – a key parameter in the stability of anion exchange membrane fuel cells. *Curr. Opin. Electrochem.* **9**, 173–178 (2018).
22. Dekel, D. R. et al. Effect of water on the stability of quaternary ammonium groups for anion exchange membrane fuel cell applications. *Chem. Mater.* **29**, 4425–4431 (2017).
23. Lyonnard, S. et al. Perfluorinated surfactants as model charged systems for understanding the effect of confinement on proton transport and water mobility in fuel cell membranes. A study by QENS. *Eur. Phys. J. Spec. Top.* **189**, 205–216 (2010).
24. Perrin, J.-C., Lyonnard, S. & Volino, F. Quasielastic neutron scattering study of water dynamics in hydrated Nafion membranes. *J. Phys. Chem. C* **111**, 3393–3404 (2007).
25. Berrod, Q., Hanot, S., Guillermo, A., Mossa, S. & Lyonnard, S. Water sub-diffusion in membranes for fuel cells. *Sci. Rep.* **7**, 8326 (2017).
26. Hanot, S., Lyonnard, S. & Mossa, S. Sub-diffusion and population dynamics of water confined in soft environments. *Nanoscale* **8**, 3314–3325 (2016).
27. FuelCellStore. Fumasep FAD-55. https://www.fuelcellstore.com/fumasep-fad-55 (2020).
28. Dlugolecki, P., Nymeijer, K., Metz, S. & Wessling, M. Current status of ion exchange membranes for power generation from salinity gradients. *J. Membr. Sci.* **319**, 214–222 (2008).
29. McGrath, M. J. et al. 110th anniversary: the dehydration and loss of ionic conductivity in anion exchange membranes due to $FeCl_4^-$ ion exchange and the role of membrane microstructure. *Ind. Eng. Chem. Res.* **58**, 22250–22259 (2019).
30. Palaty, Z. & Benndová, H. Permeability of a Fumasep-FAD membrane for selected inorganic acids. *Chem. Eng. Technol.* **41**, 385–391 (2018).
31. Marino, M. G., Melchior, J. P., Wohlfarth, A. & Kreuer, K. D. Hydroxide, halide and water transport in a model anion exchange membrane. *J. Membr. Sci.* **464**, 61–71 (2014).
32. Melchior, J.-P., Lohstroh, W., Zamponni, M. & Jalarvo, N. H. Multiscale water dynamics in model anion exchange membranes for alkaline membrane fuel cells. *J. Membr. Sci.* **586**, 240–247 (2019).
33. Melchior, J.-P. & Jalarvo, N. H. A quasielastic neutron scattering study of water diffusion in model anion exchange membranes over localized and extended volume increments. *J. Phys. Chem. C* **123**, 14195–14206 (2019).
34. Wang, L., Peng, X., Mustain, W. E. B. & Varcoe, J. R. Radiation-grafted anion-exchange membranes: the switch from low- to high-density polyethylene leads to remarkably enhanced fuel cell performance. *Energy Environ. Sci.* **12**, 1575–1579 (2019).
35. Deavin, O. I. et al. Anion-exchange membranes for alkaline polymer electrolyte fuel cells: comparison of pendent benzyltrimethylammonium- and benzylmethylimidazolium-head-groups. *Energy Environ. Sci.* **5**, 8584–8597 (2012).
36. Yassin, K., Rasin, I. G., Brandon, S. & Dekel, D. R. Quantifying the critical effect of water diffusivity in anion exchange membranes for fuel cell applications. *J. Membr. Sci.* **608**, 118206 (2020).
37. Mandal, M. et al. The importance of water transport in high conductivity and high-power alkaline fuel cells. *J. Electrochem. Soc.* **167**, 054501 (2020).
38. Chempath, S. et al. Mechanism of tetraalkylammonium headgroup degradation in alkaline fuel cell membranes. *J. Phys. Chem. C* **112**, 3179–3182 (2008).
39. Prager, M., Pawlukojc, A., Wischnewski, A. & Wuttke, J. Inelastic neutron scattering study of methyl groups rotation in some methylxanthines. *J. Chem. Phys.* **127**, 214509 (2007).
40. de Petris, S., Frosini, V., Butta, V. & Boccaredda, M. Mechanical relaxation in poly(2.6-dimethyl-l.4-phenylene oxide) in the glassy state. *Die Makromol. Chem.* **109**, 54–61 (1967).
41. Ma, Z. & Tuckerman, M. E. On the connection between proton transport, structural diffusion, and reorientation of the hydrated hydroxide ion as a function of temperature. *Chem. Phys. Lett.* **511**, 177–182 (2011).
42. Zadok, I. et al. Unexpected hydroxide ion structure and properties at low hydration. *J. Mol. Liq.* **313**, 113485 (2020).
43. Torell, L. M. & Angell, C. A. Ion-matrix coupling in polymer electrolytes from relaxation time studies. *Br. Polym. J.* **20**, 173–179 (1988).
44. Angell, C. A. Relaxation in liquids, polymers and plastic crystals — strong/fragile patterns and problems. *J. Non-Cryst. Solids* **131–133**, 13–31 (1991).
45. Gotze, W. & Sjogren, L. Relaxation processes in supercooled liquids. *Rep. Prog. Phys.* **55**, 241–376 (1992).
46. Bhattacharyya, S. M., Bagchi, B. & Wolynes, P. G. Facilitation, complexity growth, mode coupling, and activated dynamics in supercooled liquids. *Proc. Natl Acad. Sci. USA* **105**, 16077–16082 (2008).
47. Dong, D., Wei, X., Hooper, J. B., Pan, H. & Bedrov, D. Role of cationic groups on structural and dynamical correlations in hydrated quaternary ammonium-functionalized poly(*p*-phenylene oxide)-based anion exchange membranes. *Phys. Chem. Chem. Phys.* **20**, 19350–19362 (2018).
48. Meek, K. M. et al. The alkali degradation of LDPE-based radiation-grafted anion-exchange membranes studied using different *ex situ* methods. *RSC Adv.* **10**, 36467–36477 (2020).
49. Mustain, W. E., Chatenet, M., Page, M. & Kim, Y. S. Durability challenges of anion exchange membrane fuel cells. *Energy Environ. Sci.* **13**, 2805–2838 (2020).
50. Ziv, N., Mustain, W. E. & Dekel, D. R. The effect of ambient carbon dioxide on anion-exchange membrane fuel cells. *ChemSusChem* **11**, 1136–1150 (2018).
51. Dekel, D. R., Rasin, I. G., Page, M. & Brandon, S. Steady state and transient simulation of anion exchange membrane fuel cells. *J. Power Sources* **375**, 191–204 (2018).
52. Zheng, Y. et al. Water uptake study of anion exchange membranes. *Macromolecules* **51**, 3264–3278 (2018).

Publisher's note Springer Nature remains neutral with regard to jurisdictional claims in published maps and institutional affiliations.

© The Author(s), under exclusive licence to Springer Nature Limited 2022

Methods

Membrane materials and sample preparation. Fumasep FAD-55 AEMs were purchased as 10 cm × 10 cm sheets with 50–60 μm thickness from Fumatech. These polymer materials are designed to have high ionic conductance combined with mechanical and chemical stability at pH < 9. The membrane package was kept sealed until ready for use. The as-received membranes were treated in aqueous NaCl (1 wt%) at 25 °C for 24 h and subsequently washed repeatedly in ultrapure water to remove the salt, which was demonstrated by testing the conductivity of the washing water.

Samples were examined in the Br-form (to minimize the signal from Br^- during the neutron experiments) and Cl-form (to best directly compare the QENS and conductivity results) as well as substituted with OH^-. The ionic forms (OH^-, Br^- and/or Cl^-) were produced by immersing in 1 M NaOH, NaBr (aq) or NaCl (aq) at room temperature for 1 h, changing the solution three times to ensure the complete ion exchange. Each sample was washed repetitively in ultrapure water to remove excess NaOH, NaBr or NaCl, as established by testing the conductivity of the washing water.

Experiments were carried out on three H/D isotopically substituted compositions at water contents ranging between high ($\lambda = 13$) and low ($\lambda = 4$) hydration levels, expressed as the number of water molecules per functional group. The highest λ was obtained by first immersing the membrane in liquid water followed by gentle pad-drying to remove excess liquid; lower hydration was obtained by removing the appropriate amount of water using a vacuum oven (at room temperature) and heating for specified times followed by weighing. Further low-hydrated samples ($\lambda \leq 2$) were obtained by heating overnight (≥10 h) in a vacuum oven at $T = 40$ °C.

HDPE-VBC-TMA membranes with high alkaline stability and OH^- conductivity designed for AEM-FC technology were produced at the University of Surrey[34]. These samples were tested in OH-form in H_2O (following the ion-exchange procedure described above) at $\lambda = 4$.

QENS experiments. Four QENS spectrometers at three instrument facilities were used: (1) IN6-Sharp (ILL, France), to investigate relaxation dynamics on a picosecond timescale; (2) IRIS (ISIS), to study dynamics on the ten to hundred picosecond timescale; and (3) IN16B (ILL, France) and (4) HFBS (NIST, USA) to investigate nanosecond timescales. Employing spectrometers that access different timescales was necessary to carry out a full characterization of the sample dynamics.

TOF experiments were performed at 300 K using an incident wavelength of 5.12 Å (covering a Q-range between 0.3 and 2.1 $Å^{-1}$) and an instrument energy resolution E_{res} of 70 μeV (obtained by measuring the reference sample at 2 K); this configuration allows probing motions in the picosecond timescale of $0.5 < \tau < 20$ ps. Complementary experiments were performed from 230 to 325 K on IRIS, using the PG002 analyser crystal set-up ($0.56 \leq Q \leq 1.84$ $Å^{-1}$) and E_{res} of 17.5 μeV, probing motions in the range $5 < \tau < 100$ ps. IN16B experiments were performed using the standard unpolished strained Si(111) monochromator and analyser corresponding to an incident wavelength of 6.271 Å (covering a Q-range between 0.56 and 1.79 $Å^{-1}$), an instrument energy resolution of 0.75 μeV and a dynamic range of ±30 μeV; HFBS experiments were performed over a Q-range of 0.25 to 1.75 $Å^{-1}$, with $E_{res} = 1.0$ μeV and a dynamic range of ±15 μeV. These two spectrometers probe motions in the nanosecond timescale ($0.07 < \tau < 3$ ns). Any dynamical process with longer characteristic timescale will appear as 'elastic' scattering (that is, contained within the E_{res} profile) in the QENS profile, while faster processes that are accessible to the instrument contribute to a background in the QENS dataset.

EFWS data were recorded while heating (0.13 K min^{-1}; from 2 to 300 and 325 K for IN6-Sharp and IN16B, respectively) or cooling (IRIS) the sample. IFWS data were recorded either by adjusting the Doppler speed on IN16B to achieve $\Delta E = 3$ and 6 μeV energy offsets, or by integrating an arbitrarily chosen energy range (having an integration width equivalent to E_{res}; IRIS and IN6-Sharp).

AEM samples were wrapped in aluminium foil and then loaded into gold-coated flat cells (4 cm × 5 cm) or aluminium annular cells. Cells were sealed with indium. In both cases, the cells had an inner thickness of ~0.5 mm to achieve a neutron transmission of ~90%, minimizing multiple scattering. Vanadium reference and empty can measurements were carried out for data normalization (for example, detector efficiency corrections and/or data normalization to absolute units).

Ionic conductivity measurements (OH^- and Cl^- anions, partially to fully hydrated). The ionic conductivity for the FAD-55 membrane was tested for both ionic forms (OH^- and Cl^-) under fully (100% RH) and partially ($80 \leq RH \leq 65$) hydrated conditions in the temperature range from 303 to 353 K, using a BekkTech four-point probe conductivity cell.

Sample characterization. Fourier transform infrared spectra were recorded on a Bruker Alpha Fourier transform infrared spectroscopy instrument between 400 and 4,000 cm^{-1} for 16 averaged scans at 0.25 cm^{-1} resolution with autosubtracted background. Atomic force microscopy images were recorded using Bruker Dimension Icon with SNL-10A and a Scanasyst fluid+ probe. Sample imaging in water was carried out in PeakForce tapping mode. TGA was performed on a Mettler Toledo TGA/DSC 1. Samples (~5 mg) in a ceramic pan were heated from 50 to 600 °C at 10 °C min^{-1} under 60 ml min^{-1} flowing N_2, taking measurements at 1 s intervals. The raw TGA thermograms were corrected by subtraction of an empty pan measurement and normalized to their weight at 50 °C. Prior to IEC analysis, samples in Cl-form were vacuum dried at 50 °C for 4 h and the dry mass (m_d; g) recorded using a Metler Toledo Model MS204S analytical balance. Individual samples were separately immersed in aqueous $NaNO_3$ (20 cm^3, 1.2 mol dm^{-3}, large excess of NO_3^- anions), and the solutions were stirred overnight at 200 r.p.m. to exchange the Cl^- with NO_3^-. Before titration, HNO_3 (1 cm^3, 2 mol dm^{-3}) was added to the $NaNO_3$ solutions. Each solution was titrated with $AgNO_3$ (20.00 ± 0.06 mmol dm^{-3}) using the Metrohm 848 Titirino Plus auto titrator equipped with Ag Titrode. The IEC of each sample (mmol g^{-1}) was calculated from the end-point volume (EP; cm^3) and $AgNO_3$ concentration using $IEC = (EP \times 0.02)/m_d$ (ref. [34]). Raman spectra (for samples treated as described for IEC determination) were recorded using an InVia Reflex Raman Microscope (Renishaw). Spectra were recorded on five random spots on each sample surface using 785 nm excitation (100% laser power with pin in to create a spot), a ×20 objective lens (numerical aperture, 0.40) and 0.5 s exposure time. To reduce background fluorescence and improve the signal-to-noise ratio, each spectrum was acquired with a minimum photobleach of 120 s and an accumulation time of 500 s. The five spectra recorded for each sample were baseline corrected, normalized to the intensity of the 1,300 cm^{-1} peak (the poly(*p*-phenylene oxide) polymer backbone) and averaged to produce a single spectrum per sample.

Small- and wide-angle X-ray scattering and small-angle neutron scattering. Small- and wide-angle X-ray scattering profiles were acquired on a Nano-inXider instrument (Xenocs) using a micro-focus sealed-tube Cu 30 W/30 μm X-ray source (Cu Kα; wavelength, 1.54 Å). The small- and wide-angle X-ray scattering patterns (covering the Q-ranges 0.0045–0.37 $Å^{-1}$ and 0.3–4.1 $Å^{-1}$, respectively) were detected simultaneously using two Dectris Pilatus 3 hybrid pixel detectors. Scattering was collected on the same samples measured with small-angle neutron scattering and loaded in sealed capsules with Kapton windows, at room temperature and humidity. The wide-angle X-ray scattering profiles were deconvoluted using Origin2019b. Small-angle neutron scattering measurements were performed on the SANS2d beamline at the ISIS Pulsed Neutron and Muon Source (STFC Rutherford Appleton Laboratory, UK), using neutrons with wavelengths of 1.65–14 Å. Scattering profiles were simultaneously recorded on two two-dimensional detectors positioned at 4 and 8 m from the sample, providing a wide scattering vector range of $0.0025 \leq Q \leq 0.8$ $Å^{-1}$, where $Q = (4\pi/\lambda)\sin\theta$, where λ is the wavelength and θ is the scattering angle. FAD membranes were investigated after overnight treatment either (1) in a vacuum oven at 40 °C ($\lambda = 2$, where λ is the water uptake) or (2) immersed in liquid H_2O, removing the excess surface water by pad-drying the membrane surface (for example, the hydrated samples). All measurements were performed in sealed 1-mm-thick fused quartz Hellma cells at 25 °C and room humidity.

Data availability

All data needed to evaluate the conclusions in the paper are present in the paper and/or the Supplementary Information. Additional data related to this paper may be requested from the authors. Source data are provided with this paper.

Acknowledgements

In loving memory of Prof. Paul F. McMillan, a brilliant scientist and mentor, who not only inspired this work, but also his many colleagues throughout a long and proud career. F.F. acknowledges EPSRC for funding (grant EP/V057863/1). We thank the neutron scattering facilities at ILL (Grenoble, France), ISIS (Didcot, UK) and NIST (USA) for the award of beamtime necessary to carry out these experiments. We are grateful to ISIS and ILL for neutron beamtime (https://doi.org/10.5286/ISIS.E.RB1920608, https://doi.org/10.5286/ISIS.E.RB2090038-1 and https://doi.org/10.5291/ILL-DATA.9-11-1916). We also thank the Science and Technology Facilities Council for the use of the Nano-inXider instrument in the Materials Characterisation Laboratory. Access to the HFBS was provided by the Center for High-Resolution Neutron Scattering, a partnership between NIST and the National Science Foundation under agreement number DMR-2010792. Certain commercial equipment, instruments or materials are identified in this paper in order to specify the experimental procedure adequately. Such identification is not intended to imply recommendation or endorsement by NIST. This project received funding from the EU Graphene Flagship under Horizon 2020 Research and Innovation programme grant agreement no. 881603-GrapheneCore3 and from the Engineering and Physical Sciences Research Council Materials Research Hub for Energy Conversion, Capture, and Storage (M-RHEX) EP/R023581/1. F.F. acknowledges EPSRC for funding (grant EP/V057863/1). A.J.C. thanks the Society of Chemical Industry and the Ramsay Memorial Trust for support. Degradation studies performed at Surrey University were funded by Engineering and Physical Sciences Research Council grants EP/M022749/1 and EP/T009233/1.

Author contributions

The study was initiated as a collaboration between the Commissariat à l'énergie atomique et aux énergies alternatives and University College London at a meeting between P.R.S., F.F., P.F.M., S.L., G.G., Q.B. and J.-M.Z., following discussions with D.J.L.B. and T.S.M. Neutron scattering experiments were initiated and directed by F.F. and S.L. in collaboration with V.G.S., Q.B., J.-M.Z., M.A. and M.T. at neutron beamline facilities. A.J.C. and K.S. also participated in neutron scattering experiments; K.S. carried out ionic conductivity experiments under supervision from T.S.M., D.J.L.B. and

P.R.S.; A.J.C. provided Fourier transform infrared spectroscopy and TGA data; and N.M. obtained essential small- and wide-angle X-ray scattering and small-angle neutron scattering data. F.F. and P.F.M. worked closely with S.L. and Q.B. to interpret the neutron scattering results. Sample degradation, IEC determinations and Raman spectroscopy experiments were initiated and carried out by J.R.V. and A.P.P. All authors read, edited, commented on and fully contributed to developing the study and this manuscript.

Competing interests

The authors declare no competing interests.

Additional information

Supplementary information The online version contains supplementary material available at https://doi.org/10.1038/s41563-022-01197-2.

Correspondence and requests for materials should be addressed to Fabrizia Foglia or Sandrine Lyonnard.

Peer review information *Nature Materials* thanks Dario Dekel, Naresh Osti and the other, anonymous, reviewer(s) for their contribution to the peer review of this work.

Reprints and permissions information is available at www.nature.com/reprints.